Geophys. J. Int. (1995) **120,** 1–23

An arbitrary Lagrangian–Eulerian formulation for creeping flows and its application in tectonic models

Philippe Fullsack
Oceanography Department, Dalhousie University, Halifax, Nova Scotia Canada B3H 4J1

Accepted 1993 December 22. Received 1993 August 12

SUMMARY

This paper presents and analyses numerical techniques developed to investigate viscoplastic Stokes flows within a model of lithospheric deformation. In particular, the techniques are related to a subduction model of compressional orogens. The driving mechanism in the model corresponds to the near-rigid convergence and subduction of one mantle lithosphere beneath another in plane strain and this boundary condition forces flow in an overlying viscoplastic model crust. The numerical techniques use the arbitrary Eulerian–Lagrangian formulation in which flows with free surfaces and large deformation are computed on an evolving Eulerian finite-element grid that conforms to the material domain. A regridding algorithm allows the associated Lagrangian motion and fields to be followed, and, in addition, coupled back to the Eulerian calculation of the flow. Mass-flux boundary conditions are used so that the effects of erosion and deposition by surface processes, and mass loss by subduction can be included in the model calculation. The evolving model crustal layer is flexurally compensated using a general elastic beam formulation. The applicability of the numerical techniques to problems ranging from accretionary wedges to crustal and lithospheric scale deformation is discussed. Simple flows, a linear viscous subduction model, a whirl flow, and a quasi-convection model are used to show that the mass conservation, regridding and surface tracking errors are small. The broader applicability of the modelling techniques is reviewed.

Key words: arbitrary Lagrangian–Eulerian techniques, finite element, numerical techniques, subduction models, tectonics, viscoplastic flows.

1 INTRODUCTION

1.1 Continuum mechanical models of tectonic flows

The past decade has seen a growing number of attempts to model and compute tectonic flows (velocity, displacement and deformation), using continuum mechanics and numerical simulations. Studies of flows at lithospheric scale (for example, Braun & Beaumont 1987; Dunbar & Sawyer 1988, 1989), crustal- or subcrustal-scale tectonic wedges (for example, Emerman & Turcotte 1983; Stockmal 1983; Dahlen & Barr 1989; Willett 1992), at continental scale (for example, Tapponier & Molnar 1976; Vilotte *et al.* 1982) in mostly plane-strain or plane-stress conditions using thin sheet models (for example, England & McKenzie 1982; Houseman & England 1986; Vilotte *et al.* 1986; Bird 1989) have refined the plate-tectonics model at plate boundaries to help develop an understanding of the mechanics of diverse tectonic processes (for example, orogenesis or rifting). Various boundary conditions ranging from external kinematic forcing (indentor, basal motion, lateral motion, mantle plume) to more dynamically coupled models (stress-boundary conditions, surface processes, basal compensation) have been investigated. In addition, various mechanical properties have been used to provide a gross parametrization of complex and heterogeneous lithospheric materials.

In this paper additional numerical techniques to solve the underlying equations are described and analysed, and it is explained how the methods are applied to the subduction model of compressional orogens. Some aspects of the subduction model application of these techniques have already been published, for example, Willett, Beaumont & Fullsack (1993), Beaumont, Fullsack & Hamilton (1994) and Beaumont & Quinlan (1994). The primary purpose of this work is to provide the mathematical/numerical foundation

for these papers and, to avoid duplication, they are referenced extensively.

1.2 The subduction model of compressional orogens

In the subduction model of compressional orogens it is assumed that crustal-scale deformation is caused by the near-rigid convergence of the mantle lithospheres of two plates and the subduction of one beneath the other. The equivalent mechanical model (Willett *et al.* 1993; Beaumont *et al.* 1994) addresses the problem of the evolution in time of a layer of viscoplastic material attached to two underlying converging rigid plates in vertical cross-section plane-strain conditions. Fig. 1(a) shows the initial state of the layer and the steady kinematical boundary conditions that are applied to its base in order to force the shortening of the layer. We choose for convenience an external reference frame, linked to plate B, which has its origin at S, the uppermost point of contact between plates A and B (Fig. 1b). Plate A applies a driving convergence velocity V_c to the base of the layer and the applied velocity decreases over some transition length scale (0 in Fig. 1) to a zero value at point S and all locations in plate B. By comparison with natural compressional orogens, the deforming layer represents the brittle (or brittle-ductile) crust and the underlying region represents the more competent lithospheric mantles, while S represents the point at which plate A subducts under plate B. In a related analogue sandbox model (Malavieille 1984), a layer of sand is dragged by a basal sheet driven with a small horizontal velocity and pulled out through a slit at point S. In contrast to the indentor or backstop model (Davis, Suppe & Dahlen 1983; Liu, McClay & Powell 1992), in which a vertical wall is moved laterally to push the layer, the present model gives rise to a doubly vergent orogen, a feature commonly observed in continental collision zones. Because the problem is fundamentally asymmetric, we give a pro- (retro-) label to the flow or structural elements—basin, wedge, step-up shear zone—occurring upstream (downstream) of S (Willett *et al.* 1993).

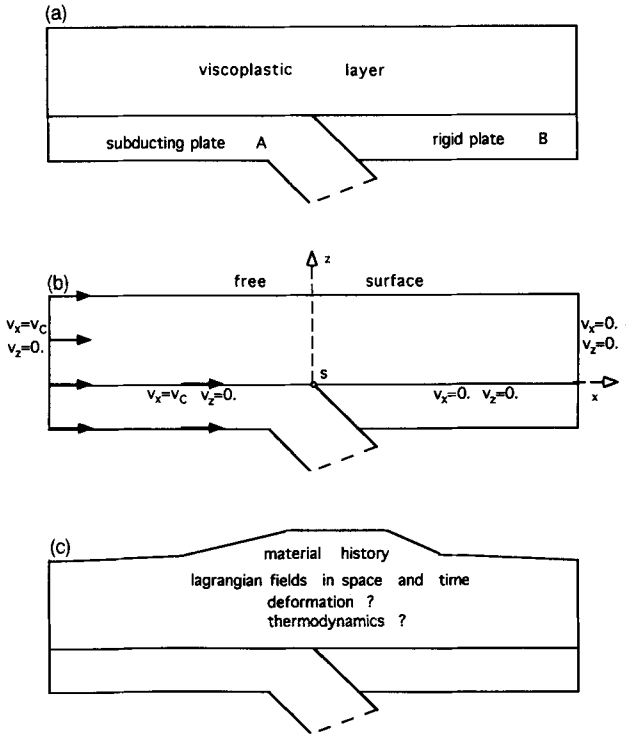

Figure 1. Basic subduction model. (a) Physical model. (b) Frame and boundary conditions. Horizontal basal velocities change from v_c on the left of the singularity point S to 0 on the right of S. We refer to the length over which the decrease in velocity is distributed as the transition length. It is zero here. (c) Results that may be computed in the numerical simulations of the model for comparison with observations. See Willett *et al.* (1993, Fig. 1) for the tectonic setting of the model.

We need a numerical treatment of not only the basic model but one which also allows us to incorporate various other boundary conditions, material types and geological processes that occur in nature and leads to a range of orogenic styles. By style, we not only mean the evolution of the model topography but the complete path in space and time of the finite deformation and thermodynamical fields (stresses, pressure, temperature; Fig. 1c). Hence we want the numerical model to handle.

(1) Various boundary conditions: advance and retreat of the subducing layer (positive and negative V_c of plate A) (roll back), double subduction, net extension, distributed mantle lithosphere compression.

(2) Various material types: rigid-plastic materials, visco-plastic materials for which the brittle/ductile transition is dynamically controlled by state parameters (e.g. pressure, temperature), strain softening and hardening.

(3) Various material distributions: e.g. initial horizontal material zonation or weak/strong inclusions.

(4) Various geological processes: erosion or deposition (surface processes) may alter the free surface, while subduction of the pro-mantle can also entrain crust into the subduction. Hence, the free surface and the basal supporting surface may be open to mass fluxes and their net shape must be tracked through time. The net thickening may be compensated by flexure of the mantle lithosphere or local isostasy (Fig. 2).

We make use of quantities related to the mass balance

$$m_l = m_A + m_E + m_S$$

in describing the subduction models, where $m_l(m_A)$ is the crustal mass input (mass accumulated) in the domain and $m_E(m_S)$ is the crustal mass leaving the domain by erosion (subduction). The quantities $m_l/\rho H^2$, $m_A/\rho H^2$, $m_E/\rho H^2$, and $m_S/\rho H^2$ are called normalized convergence, growth, erosion and crustal subduction of the model at any point in time, where ρ and H are the density and initial thickness of the crustal layer, respectively.

2 EULERIAN AND LAGRANGIAN MODEL FORMULATIONS

We now turn to the subject of continuum kinematics. Two classical descriptions of motion are the Lagrangian (L) and Eulerian (E) formulations. In the Lagrangian description the observer of the flow follows the material motion. Hence the observation and computation of velocities or flow

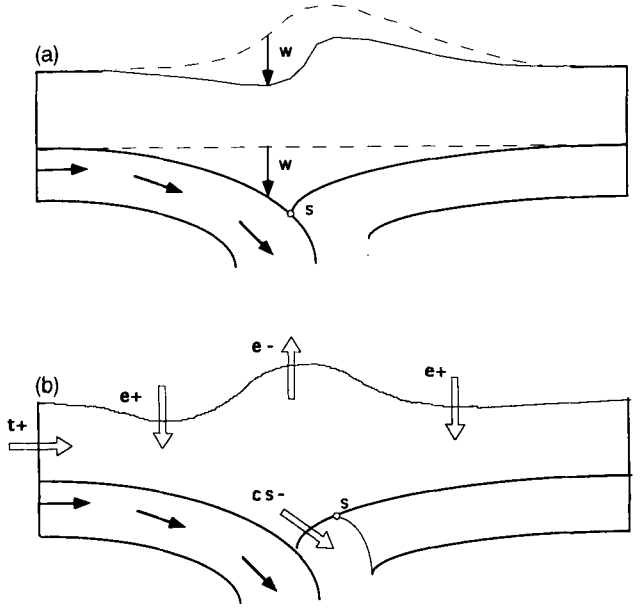

Figure 2. General subduction model. The basic subduction model (Fig. 1) can be modified by introducing isostasy and/or boundary mass fluxes. (a) Flexural or local isostasy. Every Eulerian column is displaced by the corresponding local or flexural deflection w of the base. (b) Mass fluxes crossing the boundaries may be: (1) the tectonic flux t^+ into the domain, due to tectonic convergence; (2) the deposition flux e^+ onto the domain, due to surface processes; (3) the erosion flux e^- from the domain, due to surface processes; (4) the crustal subduction flux cs^- from the domain, due to the entrainment of crustal material by the subducting plate.

increments are made at locations in space in some remote frame that are advected with the material velocity. This leads to the so-called updated Lagrangian (UL) method of numerical integration of the flow by which the mesh discretizing the medium is continuously updated in time to follow the last available prediction of current incremental motion. This approach was pioneered by McMeeking & Rice (1975) with *velocity* equations derived from Hill's variational principle. In the Eulerian description of motion, the observer of the flow is fixed in the remote frame and the discretizing mesh used in the numerical integration of the flow does not move (Eulerian (E) formulation).

A third description that generalizes the Eulerian formulation, and is the one which is used here, is the arbitrary Lagrangian–Eulerian (ALE) formulation (Hirt, Amsden & Cook 1974) in which the observers represent a non-material continuum that moves with arbitrary velocities. In contrast to the Eulerian method, ALE allows for moving material interfaces, such as free surfaces, surfaces within the domain, or its base. It has been applied to metal forming and rolling processes (Zienkiewicz & Godbole 1975). Because the ALE formulation considers both the material (or Lagrangian) medium and a non-material medium (loosely termed Eulerian), we choose the following convention (which is not the standard one). We call the velocity of the Lagrangian medium 'Lagrangian velocity', the velocity of the Eulerian medium 'Eulerian velocity', and velocity alone always means material velocity.

Each formulation has distinct advantages and drawbacks when used in a numerical solver and we briefly review a few of them.

Large strains

For infinitesimal strains no special problems arise and we, therefore, confine the discussion to examples in which the medium undergoes finite deformation. Meshes advected in a UL analysis will suffer distortion and result in loss of accuracy of, for example, the elements in a finite-element (FE) computation. ALE analysis solves this problem by minimizing mesh distortion (remaining compatible with the domain shape). The Lagrangian motion on the other hand, which involves trajectories, strains, etc., needs additional computation when using ALE because the Eulerian and Lagrangian media are distinct. A description of the computational methods used to relate the two media is given later in Section 3.

Boundary conditions

ALE methods are most convenient for the treatment of open flux boundaries. In the case of erosion or deposition of mass, for example, birth and death of elements would be a solution to the creation or removal of mass when using UL, but these change the matrix profiles. In the ALE case, however, the mesh does not have to be material and we can erode its outer shape to account for the erosion mass flux and use an arbitrary mesher inside the Eulerian domain. Consequently, surface or basal processes only require that the domain geometry be modified in a way that is consistent with overall mass conservation.

Flow type

We make a broad distinction between flows with (M) and without (WM) memory. M flows need a material integration in time. In other words, the current dynamics (rate of deformation) depends on some control quantity (which we refer to as a Lagrangian control) that is attached to the material and may be fixed in time in the material frame or accumulated by the material during deformation. WM flows are governed by equations determined solely from the current domain shape, the time-independent material type and the boundary conditions. WM pose no problem in the ALE formulation and this approach is widely used in incompressible viscous-flow computations (Ladyzhenskaya 1969). Compressibility (elasticity) puts flows in the M category by pressure (stress) control. M flows are easily integrated in UL, but there is an additional requirement in ALE to solve an advection problem because the values of the Lagrangian controls have to be recomputed on the Eulerian medium. This problem is usually cast as a first-order advection equation that is part of the equilibrium equations or is solved in staggered way with the diffusion step (Press *et al.* 1986). Special schemes, like upwind schemes or characteristics integration, are necessary to attain stability and accuracy. In the calculations described here we have opted for a more simple approach in which we replace the partial-differential equation approach by a regridding problem. We term it the ALE-R method. A UL computation could use the same technique by incorporating ALE-R steps. The elementary regridding approach we use is limited to problems in which the velocity does not change strongly on time-scales corresponding to the advection of the control fields through one element, and to Lagrangian

fields whose wavelengths are longer than the mesh resolution (this condition may deteriorate with flow advection). The method seems reasonably suited to creeping flows at low Courant–Lax–Friedrichs (CFL) numbers: $v\Delta t/\Delta x$, where v is the scale for velocity, Δt the increment of time and Δx the cell size of the discretizing mesh.

The ALE-R method is not new. It is a simple variant of the particle-in-cell methods, first developed by Harlow & Welch (1965). This class of method has long been used and brought to a high degree of sophistication in the context of plasma physics and supersonic flows (Brackbill & Ruppel 1986). It has been applied more recently to geodynamics, especially in problems involving interface advection in convective flows (Christensen 1984; Poliakov & Podladchikov 1992). For these problems, the partial-differential equation approach is an alternative and can be used in combination with effective filtering techniques (see Lenardic & Kaula 1993, which also contains a clear description of 'fitting' and 'capture' regridding methods and a useful bibliography). The potential of particle-in-cell methods lies, however, in their great generality, which could be more fully exploited to apply to any dynamical system.

Most of this paper is devoted to viscoplastic flow problems, essentially WM flows in an ALE-R formulation, and to the tracking of Lagrangian motion and material fields. The general flowchart of an ALE-R computation is given for reference in Fig. 3.

3 INTEGRATION OF CREEPING FLOWS IN THE ALE-R FORMULATION

3.1 Quasi-static motion equations

In creeping flows the acceleration is neglected, therefore, the material motion evolves through a series of equilibria:

$$\mathbf{x} = \mathbf{\Phi}(t, \mathbf{X}),$$

where the flow map $\mathbf{\Phi}$ is constrained by the current boundary conditions, conservation of mass and balance of stresses. $\mathbf{x}$ is the position at time t of a particle located at $\mathbf{X}$ at time $t = 0$. We use time stepping and solve for each interval of time $[t, t + \Delta t]$ the incremental motion $\Delta\mathbf{x}$ from the current Eulerian positions $\mathbf{x}^{\mathrm{E}}(t)$, where the current material velocity at $\mathbf{x}^{\mathrm{E}}(t)$ is $\mathbf{v} = \Delta\mathbf{x}/\Delta t$. For M flows the values ϕ^{E} at $\mathbf{x}^{\mathrm{E}}$ of all Lagrangian fields ϕ^{L} controlling the incremental motion must first be evaluated. ϕ^{E} and ϕ^{L} are the values that a physical field ϕ (for example, the temperature, the accumulated strain or the pre-stress) takes on the Eulerian medium and the Lagrangian medium, respectively.

Incompressible flows are characterized by a power dissipation function $\mathcal{h}$ and governed by the system of equations which we refer to as (S) (Sedov 1975):

$$(S)\begin{cases}\nabla\cdot\boldsymbol{T} + \rho\mathbf{g} = \mathbf{0}\\ \nabla\cdot\mathbf{v} = 0\\ \boldsymbol{T} = \dfrac{\partial \mathcal{h}}{\partial(\nabla\mathbf{v})}(\phi^{\mathrm{E}}, \nabla\mathbf{v})\\ \Sigma(\phi^{\mathrm{E}}, \boldsymbol{T}, \nabla\mathbf{v}) = 0\\ \text{BOUNDARY CONDITIONS.}\end{cases}$$

where $\boldsymbol{T}$ is the Cauchy stress tensor, ρ is the density, $\mathbf{g}$ is the gravitational acceleration and ϕ^{E} is a scalar control-like temperature, strain or strain rate, obeying an evolution equation Σ. For simplicity this equation is ignored in the rest of the paper.

Equilibrium in hypoelastic flows obeys an incremental system of equations (SI):

$$(SI)\begin{cases}\nabla\cdot\boldsymbol{T} + \rho\mathbf{g} = \mathbf{0}\\ \boldsymbol{T}^{\nabla} = \mathcal{R}(\boldsymbol{T}, \phi^{\mathrm{E}}, \nabla\mathbf{v})\\ \text{BOUNDARY CONDITIONS}\end{cases}$$

which reflects the incremental nature of the second equation, and

$$\boldsymbol{T}^{\nabla} = \frac{\Delta\boldsymbol{T}}{\Delta t} + [\dot{\mathbf{\Omega}}, \boldsymbol{T}]$$

is an objective rate of stress (like the corotational rate of Kirchoff stress or the Green–Naghdi rate of stress), where $\dot{\mathbf{\Omega}}$ is a measure of the spin rate. The thermodynamics are totally dissipative or irreversible in (S) but is partly reversible in (SI). (S) is the natural system occurring in the context of viscoplasticity and, if $\mathcal{h}$ is independent of ϕ^{E}, the flow has no memory of the past except for the evolving distribution of weight resulting from the advection process that creates the new source for pressure gradients. Although our main emphasis here is on (S) systems, ALE formulations can be used for both categories of flow. While (S) must be formulated in velocity and only integrated forward in time for incremental displacements, (SI) can be formulated either in velocity or incremental displacement. In the latter case, time stepping is limited by the convergence of the new stress balance (and in an ALE context by the accuracy of the Eulerian interpolation), and the model must be in mechanical balance at the end of each time step. The spatial integration of these systems is performed on the current Eulerian medium and in the case of (SI) needs the interpolation on this medium of the density of accumulated internal force (pre-stress). When the incremental displacement $\Delta\mathbf{u}$ is known, it is used to define a new geometry and a Eulerian motion that minimizes distortion. The Eulerian medium is then advected and the Lagrangian fields are reinterpolated on new Eulerian fields. Boundary conditions are updated and time stepping continues.

3.2 Constitutive equations

We describe here a simple family of viscoplastic rheologies. The subscripts 'D' and 'T' indicate deviatoric and trace projections and we use the following notations:

$\boldsymbol{T}$ is the Cauchy stress tensor

$T_{\mathrm{D}} = (\boldsymbol{T}_{\mathrm{D}}{:}\boldsymbol{T}_{\mathrm{D}})^{1/2}$

$\boldsymbol{D}_{\mathrm{D}} = \frac{1}{2}(\nabla\mathbf{v} + \nabla^{*}\mathbf{v})_{\mathrm{D}}$

$D_{\mathrm{D}} = (\boldsymbol{D}_{\mathrm{D}}{:}\boldsymbol{D}_{\mathrm{D}})^{1/2}$

$p = -\boldsymbol{T}_{\mathrm{T}}.$

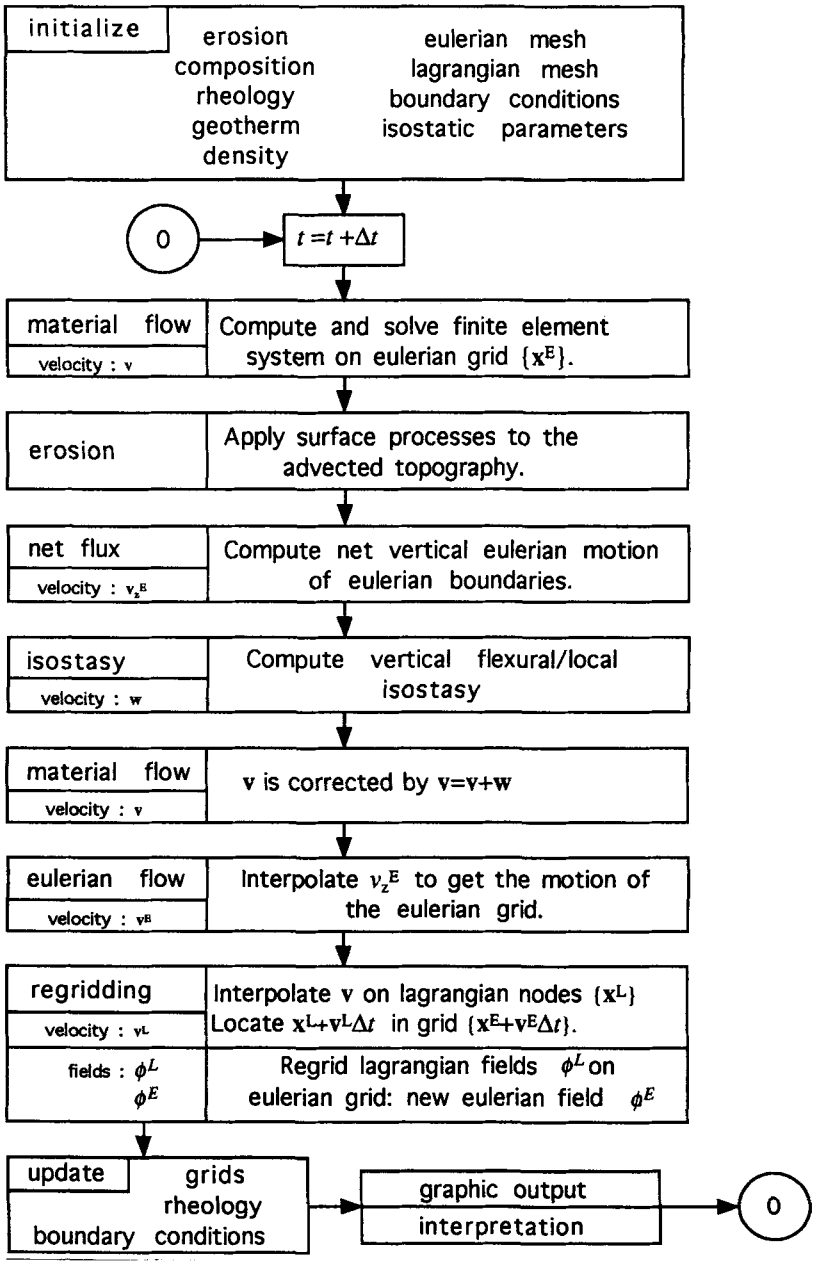

Figure 3. Flowchart of the computation for the subduction model using the ALE-R formulation. The finite-element computation is explained in Section 3 and the regridding computation in Section 4. No interpretation of the results is given in this paper. Instead, the focus is on the numerical techniques used in the model simulation.

The rheologies are parametrized by a yield function, $f(T_D, p)$, a plastic potential, $g(T_D, p)$ (Prager 1956; both functions may contain other parameters) and a viscous constitutive law, h, which may be non-linear and thermally activated as a function of the absolute temperature, θ.

If $f(T_D, p) < 0$, the material behaves as incompressible viscous with

$$D_D = h(T_D, \theta)$$

$$\text{e.g. } h(T_D, \theta) = aT_D^n \exp\left(-\frac{E + pV}{r\theta}\right)$$

where the coefficients are those normally associated with thermally activated power-law creep (Ranalli 1987, p. 269; Perzyna 1988). Hence,

$$\begin{cases} \boldsymbol{T}_D = 2\mu(D_D, p, \theta)\boldsymbol{D}_D = 2\mu_e \boldsymbol{D}_D \\ \nabla \cdot \mathbf{v} = 0 \end{cases},$$

where μ and μ_e are the viscosity and effective viscosity.

If $f(T_D, p) = 0$, the material behaves plastically with

$$\boldsymbol{D} = \lambda \frac{\partial g}{\partial \boldsymbol{T}},$$

where λ is determined by the yield equation.

We use Mohr envelopes: $f(\boldsymbol{T}_D, p) = T_D^2 + f_1(p)$. The λ parameter has therefore a unit of inverse viscosity in this convention (Fung 1965, p. 145). Any choice of $f_1(p)$ except $f_1(p) = \alpha^2 p^2$ introduces scales in the yielding process. For g we choose: $g = T_D^2 + g_1(p)$. For these 'decoupled' (f, g)

functions, the flow rule separates into two parts:

$$\begin{cases} \boldsymbol{D}_{\mathrm{D}} = \lambda \boldsymbol{T}_{\mathrm{D}} \\ \boldsymbol{D}_{\mathrm{T}} = \lambda \dfrac{\partial g_1}{\partial p}. \end{cases}$$

The material therefore behaves as a non-linear pseudo-viscous compressible fluid. If $f = g$, the flow rule is associative and automatically compressible except for constant g. Special cases are:

(Von Mises) $f_1(p) = -c^2$
$g_1(p) = f_1(p)$
c is the cohesion

(Drucker–Prager) $f_1(p) = -p^2 \sin^2 \varphi - c^2$
$g_1(p) = -p^2 \sin^2 \psi$
φ is the angle of friction
ψ is the dilatation angle

(In plane strain this criterion is equivalent to the Coulomb criterion.)

(Griffith–Murrell) $f_1(p) = -T_0 p - c^2$ T_0 is a stress scale
$g_1(p) = f_1(p)$

(Modified Cam–Clay) $f_1(p) = -(p^2 - 2pp_c)\sin^2 \varphi$
$g_1(p) = f_1(p)$
p_c is the consolidation pressure.

The Von Mises criterion models materials in the pure cohesive limit, while the other criteria show a pressure dependence that may be in better agreement with rheological observation for rocks (Jaeger & Cook 1976). Coulomb's criterion (Coulomb 1773) can be used, for example, to interpret Byerlee's law of friction. Various extensions of these plastic potentials have been proposed (for example, Hobbs, Mühlhaus & Ord 1990) to account in some parametrized way for processes like localization of deformation and dilatation. Alternative models are the double sliding model (Spencer 1964) and Cam–Clay-type models (Collins 1990). The latter class represents an attempt to construct a single, internally consistent model and has been used extensively in soil mechanics (Schofield & Wroth 1968). We note that the incompressible models we have used can generate levels of pressure that are not in any way limited by elastic or plastic compressibility and, consequently, might lead to unrealistic strength envelopes or to incorrect determinations of the dynamical brittle/ductile transition. Pressure and dilatation also directly affect velocity and stress characteristics and, hence, the interpretation of faulting angles (Mandl 1988). Consequently, we will not discuss them in detail in the context of the simple models used here. Note also that when a hardening/softening parameter is introduced (like the consolidation pressure in Cam–Clay or hardening/softening of the cohesion c, dilatation angle ψ, or friction angle φ) the yield equation does not imply a unique relation between stress and pressure but only local unicity at any point of the loading history. A distinction should, therefore, be made between stress profiles and stress envelopes in this case. More precisely, stress envelopes are particular stress profiles which assume *a priori* conditions like homogeneous strain rate, given geotherm or pressure distribution. These envelopes should not be confused with the stress profiles actually reached in the dynamical conditions of a more general physical model like the subduction model.

In our models we currently use the viscous, Drucker–Prager and Von Mises incompressible rheologies, which are the lowest-order description of the mechanical behaviour of rocks, and we neglect the role of elasticity. Our model predicts stress–strain curves that should, in principle, be compared with results from carefully monitored laboratory experiments that test a variety of boundary conditions and deformation modes (triaxial or sandbox experiments may for example be used). Until this is done, we do not know how accurate the physics of the deformation is in our numerical experiments (which happily produce strains of several 100 per cent with no dilatation or compression and a *single* yield function) in comparison with the Earth's crust. We use the basic description in the belief that it captures some of the largest-scale features of the crustal tectonic flow in conditions approximating our model boundary conditions.

The conclusion of this section is that the type of flow rule used here leads to pseudo-viscous behaviour where μ_e is the effective viscosity. From now on we focus on incompressible flows.

3.3 Spatial discretization

We use the finite-element (FE) technique to discretize our problem. By applying the virtual power principle, we retrieve the discretized equivalent of the generalized Stokes problem:

$$(S)\ \begin{cases} \nabla \cdot (2\mu_e \boldsymbol{D}) - \nabla p = -\rho \mathbf{g} \\ \nabla \cdot \mathbf{v} = 0 \\ \text{BOUNDARY CONDITIONS} \end{cases}$$

which is:

$$(S_\Delta)\ \begin{cases} \mathbf{K}_{\mathrm{D}} \cdot \mathbf{v} + \mathbf{K}_{\mathrm{T}}(p) = \mathbf{M}\mathbf{g} \\ \mathbf{K}_{\mathrm{T}}^{*}(\mathbf{v}) = 0 \\ \text{BOUNDARY CONDITIONS.} \end{cases}$$

We note * the adjoint operator, and

$$\mathbf{B} = (\mathbf{B}_1, \mathbf{B}_2 \cdots \mathbf{B}_i \cdots)$$

$$\mathbf{B}_i = \begin{bmatrix} \dfrac{\partial N_i}{\partial x} & 0 \\ 0 & \dfrac{\partial N_i}{\partial y} \\ \dfrac{\partial N_i}{\partial y} & \dfrac{\partial N_i}{\partial x} \end{bmatrix}$$

$$\mathbf{C}_{\mathrm{D}} = \frac{2\mu_e}{3} \begin{bmatrix} 2 & -1 & 0 \\ -1 & 2 & 0 \\ 0 & 0 & \frac{3}{2} \end{bmatrix}$$

$$\mathbf{C}_{\mathrm{T}} = \begin{bmatrix} -1 & 0 & 0 \\ 0 & -1 & 0 \\ 0 & 0 & 0 \end{bmatrix}$$

$$\mathbf{K}_{\mathrm{D}} = \int \mathbf{B}^{*}\mathbf{C}_{\mathrm{D}}\mathbf{B}\ \mathrm{dvol}$$

$$\mathbf{K}_{\mathrm{T}}(p) = \int \mathbf{B}^{*}\mathbf{C}_{\mathrm{T}}(p)\ \mathrm{dvol}$$

$$(\mathbf{M}_x)_{ij} = \int N_i N_j \rho\ \mathrm{dvol}$$

$$\mathbf{M}_z = \mathbf{M}_x$$

$$\mathbf{M} = \begin{bmatrix} \mathbf{M}_x & 0 \\ 0 & \mathbf{M}_z \end{bmatrix},$$

where N_i are the nodal shape functions, dvol is the infinitesimal volume element, and *ij* means the *i, j*th element of the matrix.

The saddle point problem (S_Δ) is transformed into a minimum problem by a Lagrangian constraint penalization, $p = -k\nabla \cdot \mathbf{v}$, with a value of the pseudo-bulk modulus k that is large with respect to μ_e. Merely substituting this expression in the system of equations (S_Δ) would not ensure the strong ellipticity of this problem: the pressure interpolation space must have an adequate dimension (Ladyzhenskaya 1969; Babuska 1973; Brezzi 1974). If shape functions ψ_α are introduced for the pressure, the system of equations (S_Δ) becomes:

$$(S_\Delta^1)\begin{cases}\mathbf{K}_D\mathbf{v} + \mathbf{K}_T^1 p = \mathbf{M}\mathbf{g}\\ \mathbf{K}_T^{1*}\mathbf{v} + \dfrac{1}{k}\mathbf{M}_1 p = 0\\ \text{BOUNDARY CONDITIONS}\end{cases}$$

with

$$(\mathbf{M}_1)_{\alpha,\beta} = \int \psi_\alpha \psi_\beta \,\mathrm{dvol}$$

$$(\mathbf{K}_T^1)_{i,\alpha} = \left[\int \psi_\alpha \frac{\partial N_i}{\partial x}\,\mathrm{dvol}, \int \psi_\alpha \frac{\partial N_i}{\partial y}\,\mathrm{dvol}\right].$$

For four noded elements, N_i are bilinear and pressure has one internal degree of freedom that is the element averaged pressure. Internal pressure degrees of freedom are condensed out by incomplete Gauss factorization when the element stiffness matrices are computed, yielding a stiffness matrix operating only on velocity degrees of freedoms. Equivalently selective integration of the trace (order 1) and deviatoric (order 2) parts of the matrix can be used (Malkus & Hughes 1978). Efficient discretization of the penalized problem must satisfy three requirements (Park 1984):

(1) the locking-free condition ensures velocity convergence;

(2) the divergence-free condition ensures pressure convergence;

(3) spurious or zero-energy mechanisms have to be monitored.

The 4/1 element used here satisfies the first two conditions but has a checkerboard mode at the element wavelength. When combined with a smoothing filter it has been found to be reliable enough in the present application, although oscillations may appear in the basal boundary layer near the velocity discontinuity in the subduction model. An alternative approach would be to use the 9/4 elements, which include pressure gradient degrees of freedom, but this would be at the expense of a more complex element geometry. Another, simpler, alternative would be to reconnect the discontinuous pressures by using a fully integrated pressure-mass matrix in the pressure recovery from the velocity divergence. Note that this step is important for pressure-sensitive rheologies. High penalty ratios, k/μ_e, are necessary to produce quasi-incompressibility but these lead to an ill-conditioned or even singular matrix if insufficient precision is used in the arithmetics of the computation. We have chosen here to use a high but finite penalty ratio, therefore avoiding the need to solve globally for pressures. This results in poorly conditioned linear systems that would be very difficult to solve with an iterative linear solver. This represents a strong limitation of the penalty formulation in large size (e.g. 3-D) problems.

An alternative, which we have not used here, would be to use an infinite penalty ratio. In this limit no system can be formed for the velocity alone. The pressure equations are derived from the elimination of velocities in the system of equations (S_Δ^1), and correspond to the discretization of a Laplace operator with appropriate boundary conditions. Uzawa's method of solution (Chabard *et al.* 1987) consists in applying an iterative gradient algorithm to the pressure capacitance system, an algorithm that converges to the velocity-pressure solution. Most of the methods designed to solve incompressible flow problems in the velocity-pressure variables correspond to approximations or accelerations of Uzawa's technique. Their use would be an improvement over the present penalization method.

The shape functions are built from the Eulerian grid geometry and, because the Eulerian motion does not conserve volume, the mass matrix is updated each time step to discretize the mass distribution correctly. Another reason to update the mass matrix occurs when surface processes (erosion and deposition) affect the mass balance. To reiterate, erosion feedback for WM flows in ALE-R formulation becomes a simple geometric update of the mass matrix and domain shape.

3.4 Non-linear solver

We use a particular fixed point method, direct iteration, (Zienkiewicz 1977) to solve the system of equations (S_Δ) iteratively. It belongs to the class of schemes operating on the total increment of displacement occurring in a time step by contrast with subincremental methods of the Newton type. For the non-linear rheologies used here, the algorithm essentially rescales the viscosity field locally and, as a consequence, determines the strain-rate field that is compatible with this viscosity distribution and the boundary conditions until convergence is reached. Fig. 4 shows how viscosities and material states ('viscous' under yield and 'plastic' at yield) are updated. Rigidity is penalized in rigid-plastic computations by using a high penalizing viscosity:

$$\mu_R \gg \frac{f_1(p)^{1/2}}{2D_{BC}},$$

where D_{BC} is the strain-rate scale imposed by the boundary condition (or body forces in other models) and $f_1(p)$ is estimated using the maximum static pressure. Viscosity is scaled down to its yielding value when the stresses it produces, with the current strain-rate prediction, are above the yield level. In the viscous or 'creep' regime non-linearity is characterized by the exponent n which is a function of mineral type and effective creep mechanism (for example, diffusion or dislocation climb; Perzyna 1988). We then simply use the predicted strain rate to recompute the viscosity, a procedure which, in our experience, converges for $n > 1$ (in this case the viscosity decreases when the deformation rate increases). The temperature field, θ, controlling creep activation is the Eulerian interpolation of the advected temperature field in the infinite Peclet number

1) Predictor VISCOSITY : μ_i

2) Compute VELOCITY : $K(\mu_i)\mathbf{v} = M\mathbf{g}$

3) Compute STRAIN RATE : $\boldsymbol{D}_D = (\nabla\mathbf{v} + \nabla^*\mathbf{v})/2$

$$D_D = \frac{1}{2}(\boldsymbol{D}_D : \boldsymbol{D}_D)^{1/2}$$

4) Compute PRESSURE : $p = -k\nabla \cdot \mathbf{v}$

5) Compute CREEP VISCOSITY : $\mu_v = \mu(D_D, \vartheta, p)$

6) Check if YIELDING OCCURS : $2\mu_v D_D \geq -f_1(p)$?

YES — (plastic branch) → { correct viscosity to adjust stresses to yield: $\mu_{i+1} = -f_1(p)/2D_D$; flag = plastic

NO — (viscous branch) → { $\mu_{i+1} = \mu_v$; flag = viscous

7) Corrected VISCOSITY : μ_{i+1}

Figure 4. Direct iteration method used for the determination of the effective viscosity when non-linear viscoplastic rheologies (Section 3.2) are used in the model.

case and the result of diffusion advection for a full thermomechanical coupling.

The convergence of this method is monotonic but slow and exhibits, for Von Mises and Coulomb materials, long periods with few iterations for each step interrupted by large correction steps when the viscosity field is no longer an acceptable predictor for the new stress balance. Typically three iterations for an average step and 20 or more for a large correction step are required for error levels on the velocity and the yield condition of order 1 per cent and CFL = .5.

The following are a few observations on the behaviour of the non-linear solver in the plastic context. The algorithm may fail to converge when the Gauss point or element viscosity tends to zero as a consequence of a numerical 'strain softening' positive feedback effect. This problem is not necessarily cured by choosing a minimum value that the viscosity can take because deformation may then propagate viscously along the system characteristics. This situation may be encountered near the developing pro- or retro-deformation fronts at the surface when the Coulomb criterion is used. The Coulomb envelope is singular at the surface and a minimum cohesion of a few per cent of the total layer pressure is imposed when such a problem occurs (see Beaumont & Quinlan 1994, Fig. 2c for model results). When no length-scale is imposed by the boundary conditions, the strain rate focuses along the characteristics until the grid resolution is reached. Until some form of multigrid acceleration is used to improve convergence, we accept some level of numerical diffusion to achieve reasonable computation cost. (Typical numerical costs are now comparable to a full Newton calculation because stiffness reconstruction and refactorization are needed but the element geometry is fixed and non-linearity is factorized in the viscosity array.) Points of minimum viscosity play a key role in the solution process and the algorithm appears to work, first, by searching for these points (during this phase the large wavelength part of the deformation is determined) and, secondly, by refining the active characteristics zones (this computationally costly phase operates in the small-wavelength range and may cause divergence). The large plastic deformation process can therefore be viewed as the accumulation of incremental strains on active characteristics that progressively evolve with the geometry.

In conclusion, the non-linear solution method has been reasonably successful for the limited range of applications (simple rheologies and kinematical boundary conditions) that we have investigated (Wilett *et al.* 1993; Beaumont *et al.* 1994; Beaumont & Quinlan 1994). In this context, the velocity range is known *a priori* and the problem is essentially to compute the non-linear diffusion of velocities from a known velocity source. We do not know how, in a systematic way, to prevent drifts that lead to divergence and more work is needed to optimize the solution search and to determine the solver ability to converge for hardening/softening behaviour or elasto-viscoplastic materials.

3.5 Corrections for flexural and local isostatic compensation

The subduction model makes specific assumptions about the coupling style between crust and mantle. The crust deforms in a brittle/ductile manner, with low elastic strains in comparison with the large plastic or viscous strains, under the application of the basal traction exerted by the mantle. The uppermost mantle lithosphere is assumed to maintain the convergence velocity that is imposed as a kinematical constraint and the crustal flow decouples dynamically through a boundary layer from this 'conveyor belt' motion in order to keep stresses within the stress envelope imposed by the rheology.

We decouple the crustal flow from local or regional compensation by not allowing the base of the crustal layer to deform during the crustal-flow computation. The computation is followed by a correction step which determines the vertical displacement **w** (Figs 2a and 3) due to the isostatic compensation of the net crustal thickening (i.e. thickening including the effect of erosion and crustal subduction). The

sum of these two incremental motions defines the motion $\mathbf{v}\Delta t$ used in the material advection. We also seek to investigate the effects of the mantle subduction process which accommodates the large relative displacement between the pro- and retro-mantles below the collision point S.

We use two elastic beams to model flexure of the driving pro-mantle lithosphere and the resisting retro-mantle lithosphere and connect them at their common extremity S (Fig. 2a). The deflection of the pro-mantle beam is solved first and may include the addition of an end load at S to represent the negative buoyance of the subducted material. The resulting deflection at point S is then imposed as boundary condition for the retro-mantle deflection problem. Each beam is loaded by its end boundary conditions (which can be torques, forces, displacements or rotations) and the laterally distributed differential static pressure between the crustal weight and an underlying asthenospheric fluid of density ρ_f. Tangential effects on the beam, such as those resulting from the basal traction transmitted to the crust, are ignored. Deflections obey the beam equation:

$$\kappa\nabla^4 w + \rho_f g w = \Delta(\rho_c g H),$$

where κ is the flexural rigidity, ρ_c the crustal density and $\Delta(\rho_c g H)$ the weight difference between the current and initial reference crustal column. A 1-D FE code with cubic shape functions (two nodes per element, a rotation and a deflection degree of freedom per node; Zienkiewicz 1977) computes the total deflection of each beam. Analytic tests show accurate results in the whole range of flexural parameters (i.e. from local to flexural compensation with a high flexural rigidity). Given the coarseness of the model, the non-linearity in the flexural calculation due to large deflection is not considered.

This crude technique of crust–mantle coupling will be improved in larger-scale models which will attempt to model both the crustal flow and its coupling to the two mantle corner flows associated with the subduction process. Suction effects and viscous resistance to the subduction are currently ignored and we take the view of an effectively steady-state subduction. Treating vertical compensation as an independent correction to the tectonic flow also introduces a stress disequilibrium at each timestep, but this is accounted for in the next timestep when the crustal flow increment readjusts to the compensated geometry. Boundary conditions at the mantle boundary are updated by rotating the basal velocities to align them with the tangent to the mantle boundary (when crustal subduction is not imposed, see next section).

3.6 Boundary fluxes

Erosion modifies the incremental growth flux through the Eulerian upper free surface and crustal subduction can alter what is normally a zero mass flux imposed at the mantle boundary (Fig. 2b).

Erosion

Surface processes act by modifying the weight distribution and, consequently, partly control the crustal flow, the effect being further enhanced for pressure sensitive rheologies (Beaumont, Fullsack & Hamilton 1992). We use the model tectonic velocity to both uplift and advect a 1-D or 2-D planform topography on which an erosional-depositional surface processes model operates. The resulting incremental change in height (positive for deposition) is added to the tectonic incremental displacement of the surface to find the net Eulerian motion. For planform models, strike averages of the surface processes model are used for this coupling. This approach is heuristically justified when the topographic wavelengths along strike are much shorter than those forced in cross-section by the tectonic flow, due to surface processes (Beaumont *et al.* 1992).

Crustal subduction

Entrainment of crust by the subducting slab can affect to a great extent the crustal-flow pattern, large deformation process and material histories. We again use a forced kinematical approach by imposing an exiting non-zero crustal flux through the pro-mantle boundary on some given channel width adjacent to S (Fig. 2b). The exit flux can either be constrained to be tangent to the basal boundary or can be rotated in time in the manner of an opening or closing flap to investigate forced complex tectonic episodes (for example, in the tectonic evolution of the Alps). The dynamics of the crustal subduction, including for example the interaction between channel width and lubrication (Shreve & Cloos 1986), is ignored in the present kinematics.

4 LAGRANGIAN MOTION, REGRIDDING PROBLEM

4.1 Interface tracking

An interface in the present context is either of the outer boundaries of the domain (free surface or basal boundary), or an internal interface separating different materials. The first type of interface can be, as seen previously, the locus of a mass exchange and hence be non-material. The Eulerian grid must conform to the current domain shape and may be required to respect material zonation within the domain. In many applications we use a vertical Eulerian motion (to minimize grid distortion) to track the domain boundaries and then interpolate between the new boundaries. To solve for the vertical Eulerian motion $\mathbf{v}_z^E$ of an interface, we apply the conservation of mass equation in an integral form and get a 1-D FE problem:

$$\int_\partial \langle \mathbf{v}_z^E, \mathrm{n}\rangle N_\partial \,\mathrm{dsurf} = \int_\partial \langle \mathbf{v}, \mathbf{n}\rangle N_\partial \,\mathrm{dsurf}$$

where $\mathbf{n}$ is the unit normal of the interface ∂ (evaluated at gauss points) and N_∂ are the surface shape functions. This equation simply expresses that the vertical Eulerian velocity $\mathbf{v}_z^E$ and the velocity $\mathbf{v}$ will produce the same net change of volume after advection across segments of the boundaries. Hence:

$$(S_\partial) \quad \mathbf{m}_\partial^z \mathbf{v}_z^E = \mathbf{m}_\partial^x \mathbf{v}_x + \mathbf{m}_\partial^z \mathbf{v}_z$$

with $(\mathbf{m}_\partial^x)_{i,j} = \int_\partial n^x N_\partial^i N_\partial^j \,\mathrm{dsurf}$ and $(\mathbf{m}_\partial^z)_{i,j} = \int_\partial n^z N_\partial^i N_\partial^j \,\mathrm{dsurf}$.

Clearly, the system of equations (S_∂) has a zero-flux mode at the element wavelength and this will be discussed in Section 5. The method represents a simple explicit technique to solve for the interface advection, but fails when the

interface folds over (i.e. when $\mathbf{m}_a^{\perp}$ becomes singular) as eventually happens for material interfaces in many instances. The vertical regridding must then be replaced by the Lagrangian tracking technique (for example, by assigning a different number to each material zone and regridding on the Eulerian grid the advected value of these numbers). Whether $\mathbf{m}_a^{\perp}$ is singular or not, tracking the advected interface by using Lagrangian nodes and choosing an interpolation scheme is always an alternative to (S_a) and is described below.

4.2 Lagrangian mesh advection

This section and the next one describe the details of the method used for the Lagrangian mesh advection and the regridding. A summary and an illustration are given in appendix.

An arbitrary Lagrangian grid is defined at time $t = 0$ and we call its nodes Lagrangian particles. We store the coordinates, $\mathbf{x}^{\mathrm{L}}$, of each Lagrangian particle and the number, I, of the Eulerian element that contains it ($I \leq 0$ when the particle is outside the Eulerian domain). When the incremental flow $\mathbf{v}$ has been determined on the Eulerian grid (including beam deflection), we update $\mathbf{x}^{\mathrm{L}}$ and I with the following simple algorithm. From $\mathbf{x}^{\mathrm{L}}$ and the vector of coordinates $\mathbf{x}^{\mathrm{I}}$ of all Eulerian nodes defining I we write, using the FE shape functions matrix $\mathbf{N}(\mathbf{r})$, the system of equations:

$$(SN) \quad \mathbf{x}^{\mathrm{L}} = \mathbf{N}(\mathbf{r})\mathbf{x}^{\mathrm{I}}.$$

The system (SN) simply states that $\mathbf{x}^{\mathrm{L}}$ is the image of $\mathbf{r}$ from the reference domain through the interpolation map. This relation is inverted for the vector $\mathbf{r}$ and the Lagrangian velocity $\mathbf{v}^{\mathrm{L}}$ is found by the same mapping (isoparametric interpolation) from the vector of material velocities at the nodes of the Eulerian element I (these do not include an erosion or deposition correction for the surface processes). Then, by forward Euler integration:

$$\mathbf{x}^{\mathrm{L}}(t + \Delta t) = \mathbf{x}^{\mathrm{L}}(t) + \mathbf{v}^{\mathrm{L}}\Delta t.$$

A local search process begins around I to determine which new Eulerian element, I_1, contains the advected Lagrangian position. To decide if a particle belongs to an element, we choose between either a direct check in $\mathbf{x}$ space or a new inversion of the system (SN) using the advected position and the test element. The particle is in, or out, depending on whether its reference image does, or does not, fall in the reference domain. Elements adjacent to the boundaries are slightly dilated outwards to account for the unavoidable mismatch between the Eulerian and Lagrangian boundaries due to numerical errors, which occurs even in the absence of erosion or subduction fluxes. For these boundary elements, the reference vector $\mathbf{r}$ is projected back to the boundary of the reference domain to avoid extrapolation of the velocities outside the Eulerian grid. Usually, the local search succeeds for good Eulerian grid designs and CFL < 1, but when it fails a second broader search is used. Clearly, instances where particles cross several Eulerian elements in one timestep should be avoided because the Lagrangian advection would not use the full resolution of the velocity field computed on the Eulerian grid. When this broader search also fails, it implies that the particle has left the domain and its Eulerian element number is reversed in sign. Particles can only cross the boundaries as a result of erosion or subduction and when this occurs the now dummy particle is advected arbitrarily, e.g. with the velocity it had when crossing the Eulerian boundary.

If Lagrangian fields are to be interpolated on the Eulerian grid, the Lagrangian grid must at all times cover the entire Eulerian domain. This is achieved either by the regular injection of new Lagrangian particles, where there is influx to the domain, or by defining an initial large Lagrangian grid whose nodes will progressively enter the domain.

In addition to the entry flux, deposition on the boundary by surface processes represents a second material source. This sedimentary mass is regularly incorporated into the model by adding to, or 'coating', the Lagrangian grid with a new layer of nodes whose position coincides with the Eulerian surface nodes at the time of deposition. The line of nodes is then advected with the standard procedure explained above and may later be buried by subsequent deposition or partially exhumed by subsequent erosion. This procedure can be used to record the syn-orogenic sediment stratigraphy in models coupling tectonic and surface processes (Johnson & Beaumont 1994).

4.3 Regridding problem

In Section 2 the ALE-R formulation was defined as a fractional step method that alternates a diffusion-production substep on the Eulerian grid and an advection substep performed by regridding fields ϕ^{L} defined on the Lagrangian grid, onto fields ϕ^{E} defined on the Eulerian grid. We have used the three most elementary methods for the regridding operation:

(1) symmetric nodal interpolation—Lagrangian fields are consistently interpolated from Eulerian nodal values and, symmetrically, Eulerian nodal values are consistently interpolated from Lagrangian nodal values.

(2) Closest point nodal 'interpolation'—the value of ϕ^{E} at Eulerian nodes is the value of ϕ^{L} at the closest Lagrangian node (we use CP to denote this operator).

(3) Element mixing of nodal values—ϕ^{E} is constant per element and takes the average value of all nodal Lagrangian values inside the element.

We may loosely distinguish two classes of advection methods: conservative methods, which are designed from a conservation principle and more general interpolation methods. A good scheme should be both conservative and minimize diffusion and dispersion errors (Lenardic & Kaula 1993). Our schemes belong to the second category and define the regridding operator by a linear equation:

$$\phi^{\mathrm{E}} = \int \phi^{\mathrm{L}} w_{\mathrm{L}}^{\mathrm{E}} \, \mathrm{dvol},$$

with particular values of the weight functions $w_{\mathrm{L}}^{\mathrm{E}}$ and definitions of the approximation spaces for ϕ^{E} and ϕ^{L}. No correction filter enforcing conservation has been applied at this stage. If the field ϕ obeys an evolution equation with non-zero Peclet number, a new diffusion-production increment $\Delta\phi_{\mathrm{DP}}^{\mathrm{E}}$ is computed on the Eulerian grid. The

operator regridding $\phi^E + \Delta\phi^E_{DP}$ onto ϕ^L is simple the Eulerian isoparametric interpolator.

Resolution

The simplicity of these techniques is in contrast to all other more elaborate methods developed to solve the advection problem. The best approach for given levels of robustness, accuracy and computational cost is probably problem dependent, but the control of resolution is central and therefore warrants some discussion.

Regridding is only exact when the trivial UL formulation is used, but in this case the solution rapidly becomes inaccurate because grid advection causes loss of resolution in velocity gradients in the areas of flow divergence and an additional loss of accuracy due to the FE element distortion. Regridding generally involves a projection on the changing approximation space and cannot be consistent. Advection by the flow is essentially non-linear and modifies each error source and, in particular, the discretization error. A material discretization error is defined as the maximum distance between linear segments linking initially adjacent Lagrangian particles and the current material line connecting these particles. The material discretization error is zero for linear flows and evolves generally as a function of time and velocity curvature (e.g. exponentially for flows with positive Lyapounov exponents). Material discretization errors measure the loss of material connectivity of the Lagrangian grid. It can be estimated, for example, from the error between computed and interpolated trajectories of the Lagrangian element centres. Symmetric nodal interpolation becomes inaccurate as soon as the material discretization error exceeds the Eulerian resolution. We therefore favour the other two schemes, which moreover, can be performed by forward bookkeeping inside the loop updating the Lagrangian nodal positions, although these are also sensitive to the material discretization error. The choice of numerical parameters (CFL, Eulerian and Lagrangian discretizations) should maintain a balance between the resolution of the physical model, δ^P, the resolution of the Lagrangian grid, δ^L, and the resolution of the Eulerian grid, δ^E. An example of physical resolution is the scale at which the model fails to be homogeneous. Using continuum mechanics, homogeneous rheologies set limits to the physical resolution and the process of large deformation might itself alter the necessary physical resolution (e.g. for localization or strain softening) unless diffusion processes limit the small wavelength gradients.

In conclusion our regridding method is limited by: first, drift of the material discretization error (which requires either very dense initial Lagrangian clouds or the injection of new Lagrangian nodes), and second, the lack of Eulerian node motion (and injection mechanism) which would adapt the Eulerian grid to the flow (Hawken, Gottlieb & Hansen 1991).

5 NUMERICAL EXAMPLES

In this section numerical errors are discussed in a semi-quantitative way, i.e. without formal analysis. The methods are analysed for their numerical aspects without special consideration to the application. The emphasis is on mass conservation and errors associated with the interface tracking and regridding processes. The basic subduction model is used in a test of the interface tracking but two different models, the whirl flow (Ottino 1989) and a quasi-convection flow will be used in the discussion of the regridding. As noted in the introduction, examples of results of the subduction model and its elaborations can be found in Willett *et al.* (1993), Beaumont *et al.* (1994) and Beaumont & Quinlan (1994).

5.1 Mass conservation

Several sources of error explain why mass conservation can only be approximated and we have estimated them using the following quantities as indicators:
$m_I(t) = V_c t$ is the total mass input in the domain in the time inverval $[0, t]$;
$\Delta m_I(t) = V_c \Delta t$ is the incremental mass input in $[t, t + \Delta t]$;

(1) $\Delta m_P(t) = \left(\Delta t \int_{\{\mathbf{x}_t\}} \nabla \cdot \mathbf{v}\, \mathrm{dvol}\right) \Big/ \Delta m_I(t)$

is the penalty error due to the finite ratio k/μ_c;

(2) $\Delta m_A(t) = \left(\int_{\{\mathbf{x}_t + \mathbf{v}\Delta t\}} \mathrm{dvol} - \int_{\{\mathbf{x}_t\}} \mathrm{dvol}\right) \Big/ \Delta m_I(t)$

is the error due to the finite advection that occurs in $[t, t + \Delta t]$.

As $\nabla \cdot \mathbf{v}$ is only a first-order approximation of the average rate of change of the Jacobian during a finite period of time, Δm_A differs from Δm_P;

(3) $\Delta m_{NL}(t) = \Delta m_A(t) - \Delta m_P(t)$ is the non-linear part of the error $\Delta m_A(t)$;

(4) $\Delta m_S(t) = \left(\int_{\{\mathbf{x}_t + \mathbf{v}\Delta t\}} \mathrm{dvol} - \int_{\{\mathbf{x}_t\}} \mathrm{dvol} - \Delta m_I(t)\right) \Big/ \Delta m_I(t)$

is the total mass error in $[t, t + \Delta t]$;

(5) $\Delta m_T(t) = \left(\int_{\{\mathbf{x}_t\}} \mathrm{dvol} - \int_{\{\mathbf{x}_0\}} \mathrm{dvol} - m_I(t)\right) \Big/ m_I(t)$

is the total accumulated mass error in $[0, t]$;

(6) $\Delta m_R(t) = \left(\int_{\{\mathbf{x}_t + \mathbf{v}^E \Delta t\}} \mathrm{dvol} - \int_{\{\mathbf{x}_t + \mathbf{v}^E \Delta t\}} \mathrm{dvol}\right) \Big/ \Delta m_I(t)$

is the mass error that occurs in $[t, t + \Delta t]$ as a consequence of the Eulerian regridding.

We have assumed that density was initially uniform to simplify the discussion. If surface processes or other sources of flux, like crustal subduction, are coupled to the flow model, their mass balance is computed and the mass balance indicators are modified accordingly. Local mass conservation can also be used, for example, to test if the computed Lagrangian motion has departed from material motion and it, therefore, provides a criterion for the addition, or injection, of Lagrangian nodes.

5.2 Interface tracking

In this section the linear viscous subduction model is used to test and compare three different methods (A, B, C) for the Eulerian free surface tracing and the Eulerian grid motion.

The model is run in the high viscosity or, equivalently, low gravity limit. This corresponds to the case where forces produced by viscous shear are much higher than forces due to gravity, in short we use a dimensionless 'viscosity' $R_v = \mu\dot{\varepsilon}/\rho g h = 100$. This model is closely related to the corresponding flat (180° angle) corner flow model. However, in the present example the free surface upper boundary condition imposes a length-scale for the diffusion of velocities from the velocity source given by the lower boundary condition. The problem has a purely geometric solution but not a stationary solution because no time-scale exists for relaxation.

Method A

This approach combines the simple computation described in Section 4.1 for the Eulerian free surface tracking and vertical Eulerian motion. The tracking algorithm is purely explicit in time. As noted earlier, an unstable element wavelength, zero flux mode is present in the matrix of the system and grows exponentially with a time-scale dependent of the CFL number in the region where horizontal transport is dominant over the vertical uplift source, i.e. from the influx boundary condition. Experiments with artificial diffusion computed with the CFL number show that this mode can be damped but at the expense of a loss of accuracy. For example, the introduction of diffusion in the determination of the Eulerian free surface creates significant errors between the Eulerian and the material boundaries, especially for topographies with strong curvature.

Method B

In this method the Eulerian motion is also vertical, but the top line of Eulerian nodes is first advected and cubic-spline interpolation (Press *et al.* 1986) is used to determine the Eulerian vertical displacement. This method was tested to see how an arbitrarily chosen interpolator would perform in comparison with a potentially more conservative method, such as A.

Method C

In this method the Eulerian motion follows the velocities at the free surface and is obtained by vertical linear interpolation or pure shear. Therefore, the motion also has a varying horizontal component and the Eulerian grid is correspondingly compressed below the high curvature areas of the free surface.

All runs were performed on a 200×10 grid in 16 bit arithmetic, with a penalty ratio = 1000, CFL = 0.5, until a normalized convergence of four has been reached. Fig. 5 shows the different mass error indicators defined in Section 5.1. The penalty error (error estimate 1, Fig. 5) is, as expected, of the order of the inverse of the penalty ratio. The finite advection error (error estimate 2, Fig. 5) is largely dominated by its non-linear component that scales like the incremental displacement per step. Doubling CFL for the same discretization doubles this error, and using a 50×10 grid at CFL = 0.5 quadruples it. This error source could be reduced by using a higher-order representation of the finite volumetric strain, like the midpoint strain computed on the midpoint configuration for the period $[t, t + \Delta t]$, or equivalently, by using a Runge–Kutta method. The regridding mass error (error estimate 6, Fig. 5) is of course zero for method C but shows a slight drift due to the higher-order interpolation when method B is used.

Method A behaves in a different way and it can be seen that the regridding error corrects almost exactly the non-linear advection error. Although we do not have a clear explanation for this behaviour, we think that it is peculiar to the boundary conditions used here and suggest the following interpretation. The sign of the non-linear advection error (error estimate 3, Fig. 5) is controlled by the angle between the velocity and the strain-rate orientation and artificial dilatation (compression) occurs on the retro- (pro-) side; an error symmetry in sign when tracking the topography could account for a diminished total mass error. The total mass error (error estimate 5, Fig. 5) has for this reason been found to be systematically lower for method A than for method B (when growth of the unstable mode in A was eliminated). As already mentioned, unstable oscillations may occur with method A and need stabilization by artificial diffusion. Such Lax schemes (Press *et al.* 1986) have been used to modify method A but did not systematically meet the stability and accuracy requirements.

Overall, method B seems to be more robust than A, even though A gives a four times better Eulerian mass balance for this particular series of tests. Both the advection mass error that affects the Lagrangian motion and the regridding will need further improvement for higher accuracy.

Figure 6 shows the corresponding evolution of the Eulerian free surfaces (lines) and the updated positions of a set of Lagrangian nodes (X's) originally positioned on the initial free surface. The Eulerian surface motion is seen to be in close agreement with the material motion. We have computed the differences in x and z components of displacement resulting from the different methods after 400 per cent normalized convergence and scaled them by the convergence. The notation Δx_{AB} typically means $\max(x_A - x_B)$ where A, B, and C are the methods, pro- (retro-) locations are labelled by 'P(R)', and 'L(E)' identifies whether Lagrangian (Eulerian) advections are compared:

$${}^{L}\Delta x^{P}_{BC} = 2.8\% \qquad {}^{L}\Delta x^{R}_{BC} = 3.6\%$$

$${}^{L}\Delta z^{P}_{BC} = 1.6\% \qquad {}^{L}\Delta z^{R}_{BC} = -3.2\%$$

$${}^{L}\Delta x^{P}_{AC} = 2.0\% \qquad {}^{L}\Delta x^{R}_{AC} = 3.6\%$$

$${}^{L}\Delta z^{P}_{AC} = 3.6\% \qquad {}^{L}\Delta z^{R}_{AC} = -3.6\%$$

$${}^{L}\Delta x^{P}_{AB} = 0.8\% \qquad {}^{L}\Delta x^{R}_{AB} = 2.0\%$$

$${}^{L}\Delta z^{P}_{AB} = -0.6\% \qquad {}^{L}\Delta z^{R}_{AB} = 0.6\%$$

$${}^{E}\Delta z^{P}_{AB} = -2.0\%$$

$${}^{E}\Delta z^{R}_{AB} = 12.0\%$$

The numbers are maxima and the errors are typically one order of magnitude smaller than these values.

It should be appreciated that the example shown here is computationally easier than models that use more complex boundary conditions or rheologies. Both time and convective accelerations are, for example, very low as can be

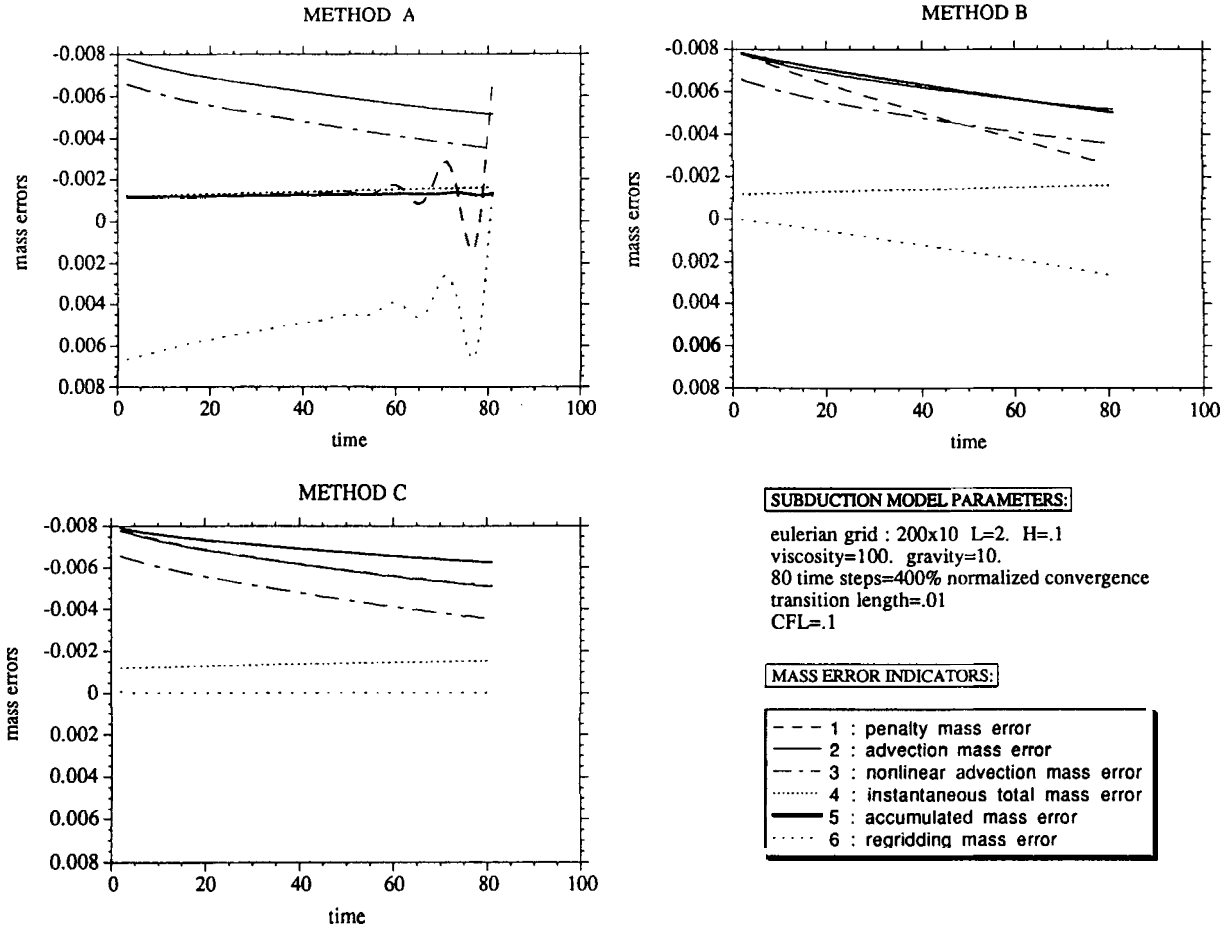

Figure 5. Interface tracking. Evolution through time of the mass-error indicators defined in Section 5.1 for three methods (A, B, C) of tracking the free surface. Method A: flux formulation (Sections 4.1 and 5.2). Method B: cubic-spline interpolation (Section 5.2). Method C: horizontal Eulerian advection (Section 5.2). The linear viscous subduction model is applied to a layer of height $h = .1$ and width $L = 2$. See the caption of Fig. 1 for the definition of the transition length.

seen in Fig. 6. Plastic subduction models, for example, produce strain-rate zones at the Eulerian resolution limit and, correspondingly, high curvature points on the topography (Beaumont & Quinlan 1994 Fig. 2c). This effect is cumulative on the retro-side where the direction of advection is close to the direction of shearing. When the front of deformation progresses slowly, the velocity gradients force Lagrangian particles to accumulate in an Eulerian cell. A close analogy is a velocity field that takes two different constant values on each side of a fixed location on the surface. In this case, the horizontal advection does not relax the velocity values exponentially as it should because of the explicit time integration and the Lagrangian surface can fold over. On the other hand, the Eulerian surface continues to be tracked on average for wavelengths larger than the Eulerian mesh resolution. If the Eulerian mesh is allowed to compress near deformation fronts, complete loss of stiffness may occur, resulting in a zero velocity field.

5.3 Lagrangian advection and regridding: methods

The ALE-R method relies on a time integration and two interpolation processes between Eulerian and Lagrangian nodes, and we have presented a basic version of these components in Section 4. All applications of the subduction model that we have referred to so far have used forward Euler integration in time and either closest-point interpolation or element mixing for the regridding to the Eulerian grid in the cases where temperatures were used, in the advective limit, to activate creep. This technique was also used to track material zones in models (Beaumont *et al.* 1994) which assume that the crust has a heterogeneous rheology. However, the combination of a first-order time integration and a regridding using a fixed-size Lagrangian grid may give low accuracy in space and time. We show here slight modifications of the basic regridding scheme described in Section 4 and test this improved scheme on an analytical example and an M flow (Section 2).

Time integration

Forward Euler integration of trajectories neglects both the variation in time of the velocity field due to the temporal changes in dynamics and the variation in time of velocities induced along the trajectories by the advection through a spatially varying velocity field. Higher accuracy is obtained by using an implicit trapezoidal discretization: if x^L is the

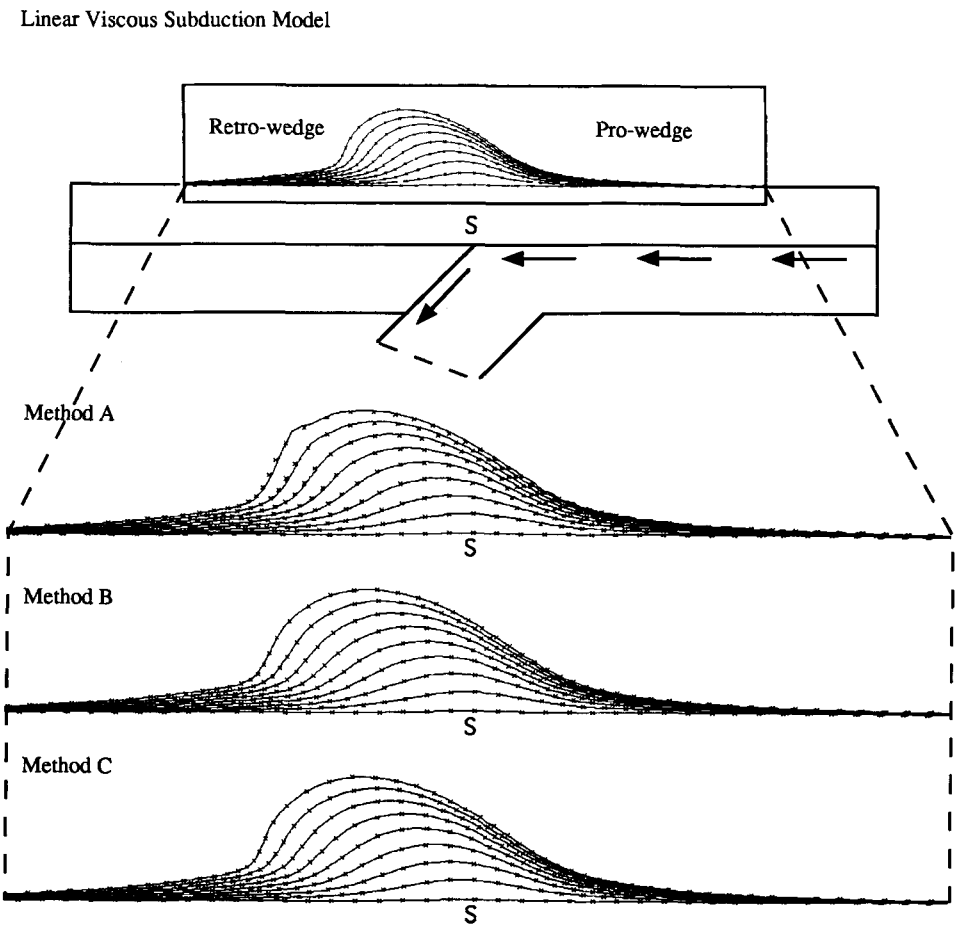

Figure 6. Interface tracking. Evolution through time of the Eulerian free surfaces (lines) and advected Lagrangian nodal positions (crosses) for the surface tracking methods A, B, C used in Fig. 5. Surface positions are shown for 50 per cent increments in the normalized convergence (as defined in Section 1.2). Eulerian nodes are not shown. The initial positions of the Lagrangian nodes are shown in the figure on the horizontal lines. Note that: (1) at any time, the Lagrangian positions are close to the current Eulerian free surface; and (2) the results of the three methods are almost identical (see Section 5.2). Note that, unlike Fig. 1, the pro-side is on the right. The retro-wedge is steeper than the pro-wedge, but this asymetry may reverse for lower viscosities (not shown here).

Lagrangian particle whose trajectory is being solved for in the time interval $[t, t+\Delta t]$, then

$$\frac{d\mathbf{x}^{\mathrm{L}}}{dt} = \mathbf{v}(\mathbf{x}^{\mathrm{L}}, t)$$

can be approximated by

$$\mathbf{x}^{\mathrm{L}}_{n+1} - \mathbf{x}^{\mathrm{L}}_{n} = \frac{\Delta t}{2}[\mathbf{v}(\mathbf{x}^{\mathrm{L}}_{n}, t) + \mathbf{v}(\mathbf{x}^{\mathrm{L}}_{n+1}, t+\Delta t)].$$

For WM flows the Lagrangian advection can be computed when velocities are known for the period $[t+\Delta t, t+2\Delta t]$. For M flows we assume that velocities are stationary in time and get:

$$\mathbf{x}^{\mathrm{L}}_{n+1} - \mathbf{x}^{\mathrm{L}}_{n} = \frac{\Delta t}{2}[\mathbf{v}(\mathbf{x}^{\mathrm{L}}_{n}, t) + \mathbf{v}(\mathbf{x}^{\mathrm{L}}_{n+1}, t)].$$

This poorer approximation still provides a significant correction when accelerations in time due to the changing dynamics are smaller than spatial or convective acceleration.

Either equation is solved by a fixed-point method which converges if $\|\Delta t/2\nabla\mathbf{v}\| < 1$. This modification gives to the Lagrangian trajectory a convective acceleration that increases accuracy in Space. Spatial variations of velocities within or across Eulerian elements are taken into account in this algorithm.

We reiterate that the regridding algorithm works in essentially the same way whether a velocity or incremental displacement formulation is used for the equilibrium equations. In the latter framework, which is the basis of most elasto-viscoplastic solvers, the Lagrangian advection is simply performed by consistent interpolation because time integration is implicit in the determination of the new equilibrium.

Spatial interpolation

We use the Eulerian consistent interpolation to determine nodal Lagrangian values but several choices are possible for the interpolation from Lagrangian nodes to Eulerian nodes. These choices depend on whether a cloud or a grid structure is assigned to the Lagrangian nodes and we briefly discuss the respective merits of each approach.

Both structures track the transport but grids need more bookkeeping especially when adaptive grid refinement is

needed because connectivities change in the course of deformation. On the other hand, the grid structure allows the determination of quantities like finite strain or length stretch and also provides an interpolation basis, for example, to perform symmetric bilinear interpolation. Clouds are simpler to handle and might be better adapted to mixing flows or flow regimes where only statistical measures of material configurations are available or relevant. In this case, however, the regridding must be associated with the computation of effective material properties at the Eulerian grid resolution, a question which will not be considered here.

We now describe a particular cloud method that uses closest point interpolation (CP) and injection of new Lagrangian particles. CP could be replaced by a method weighting the Lagrangian values by a function of their distance to the Eulerian node, this function being zero outside some small disc centred at the Eulerian node to keep the interpolation local. Automatic injection of Langrangian particles is performed, based on the following bisection equations:

$$\mathbf{x}^{\mathrm{L}}_{\mathrm{new}} = \frac{\mathbf{x}^{\mathrm{E}} + \mathrm{CP}(\mathbf{x}^{\mathrm{L}})}{2} \qquad \text{(position)}$$

$$\theta^{\mathrm{L}}_{\mathrm{new}} = \tfrac{1}{2}(\theta^{\mathrm{E}} + \mathrm{CP}(\theta^{\mathrm{L}})) \qquad \text{(temperature)}$$

when the distance of the Lagrangian cloud to the Eulerian grid exceeds some limit $\delta_x(\delta_z)$ in the x- (z-) direction. We could alternatively define the new nodes at the Eulerian location. Both the time integration and the interpolation are performed in the same forward loop over Lagrangian particles. We always choose CFL < 1, therefore every computation is local to the Eulerian cell and its eight neighbours. Consequently, the algorithm is suited for vector and parallel computation by numbering the Eulerian cells into nine groups of non-adjacent cells. The loop over the nine groups is sequential, but each group is totally disconnected and gather-scatter operations or distribution of computations to a large array of processors are possible and a gain of time of order nine can be expected, where n_{E} is the number of Eulerian elements.

5.4 Lagrangian advection and regridding: examples

An analytical example: the whirl flow

The whirl flow (Ottino 1989) is a flow with rotational symmetry in which concentric layers of material rotate around a centre with an angular velocity that has a single maximum at some finite distance r_0 from the centre. In this example a stationary velocity field is defined, on a fixed Eulerian grid of size 60×60, with the angular velocity distribution

$$\dot{\omega}(r) = \dot{\omega}_0 \frac{r}{r_0} e^{-r/r_0}$$

in the box $[-0.5, +0.5] \times [-0.5, +0.5]$, where r is the distance to the origin, $r_0 = 0.25$ and $\dot{\omega} = 0.3$. These parameters give a minimum period of rotation $\tau_{r_0} \sim 60$, and a value $\Delta t = 1.0$ is chosen for the time step. An initial regular grid of 60×60 Lagrangian particles is chosen in the smaller box $[-0.3, +0.3] \times [-0.3, +0.3]$ in order to increase the Lagrangian resolution and prevent particles from leaving the Eulerian domain.

We examine first the advection and second the regridding errors.

(1) The exact advection of the initial Lagrangian grid is computed and compared to the numerical advection of the same grid. For the numerical advection the trapezoidal method is used because forward Euler integration gives divergent spiral trajectories that rapidly drift from the solution. The maximum absolute displacement error is observed to increase linearly at a rate of 2.5×10^{-5}, giving a maximum error of 5×10^{-3} (a third of the Eulerian resolution) after 200 steps.

(2) Differential rotation creates shearing and any field ϕ without rotational symmetry is eventually mixed at progressively smaller scales by the whirl flow. This can be demonstrated by choosing an initial field $\phi(x, z, 0) = x$, corresponding to a homogeneous gradient in the x-direction at time $t = 0$. The analytical solution for the Eulerian value $\phi^{\mathrm{E}}(x, z, t)$ of the field advected by the flow at time t is:

$$\begin{aligned}\phi^{\mathrm{E}}(x, z, t) &= x \cos(\dot{\omega}(r)t) + z \sin(\dot{\omega}(r)t) \\ &= \cos(\dot{\omega}(r)t + \varphi(x, z))\end{aligned}$$

where $x + iz = r \exp(i\varphi(x, z))$ in complex notation.

The x-gradient $\partial\phi^{\mathrm{E}}/\partial x$ evolves in time like:

$$\frac{\partial \phi^{\mathrm{E}}}{\partial x} = \cos(\dot{\omega}(r)t) + \frac{x}{r_0}\dot{\omega}_0 t\left(1 - \frac{r}{r_0}\right)e^{r/r_0} \sin(\varphi(x, z) - \dot{\omega}(r)t).$$

We therefore see that the amplitude of x-gradients tends linearly to $+\infty$ or $-\infty$ with time for every point in space (except for $r = 0$, $r = r_0$ and $r = +\infty$) at a rate that depends on the location (x, z). Similar calculations apply to z-gradients.

The error due to CP regridding is expected to behave like:

$$\Delta\phi^{\mathrm{E}} \sim \delta^{\mathrm{CP}} \|\bar{\nabla}\phi^{\mathrm{E}}\|,$$

where δ^{CP} is the distance of the closest Lagrangian point to the Eulerian node. The function δ^{CP} is clearly time periodic in the case of the whirl flow and its maximum amplitude depends on the initial Lagrangian resolution. This behaviour is confirmed in Fig. 7, which shows the comparison between the analytical solution $\phi^{\mathrm{E}}(x, z, t)$ and its numerical value $\hat{\phi}^{\mathrm{E}}(x, z, t)$ for the three arbitrarily chosen Eulerian locations on the segment $[0, r_0]$ of the x-axis:

$(x_1, z_1) = (.20r_0, 0.)$ (Fig. 7a)

$(x_2, z_2) = (.40r_0, 0.)$ (Fig. 7b)

$(x_3, z_3) = (.60r_0, 0.)$ (Fig. 7c).

The number of flow cycles in the time period $[0, 200]$ at these Eulerian locations are respectively 1.57, 2.57 and 3.16. The short wavelength component of $\hat{\phi}^{\mathrm{E}}$ (Fig. 7) due to the regridding process is the combination of two effects: a reduced number of points per wavelength for small radius (e.g. Fig. 7a) and the linear increase of the noise amplitude with time, noted above, at a rate which decreases as $r = r_0$ is

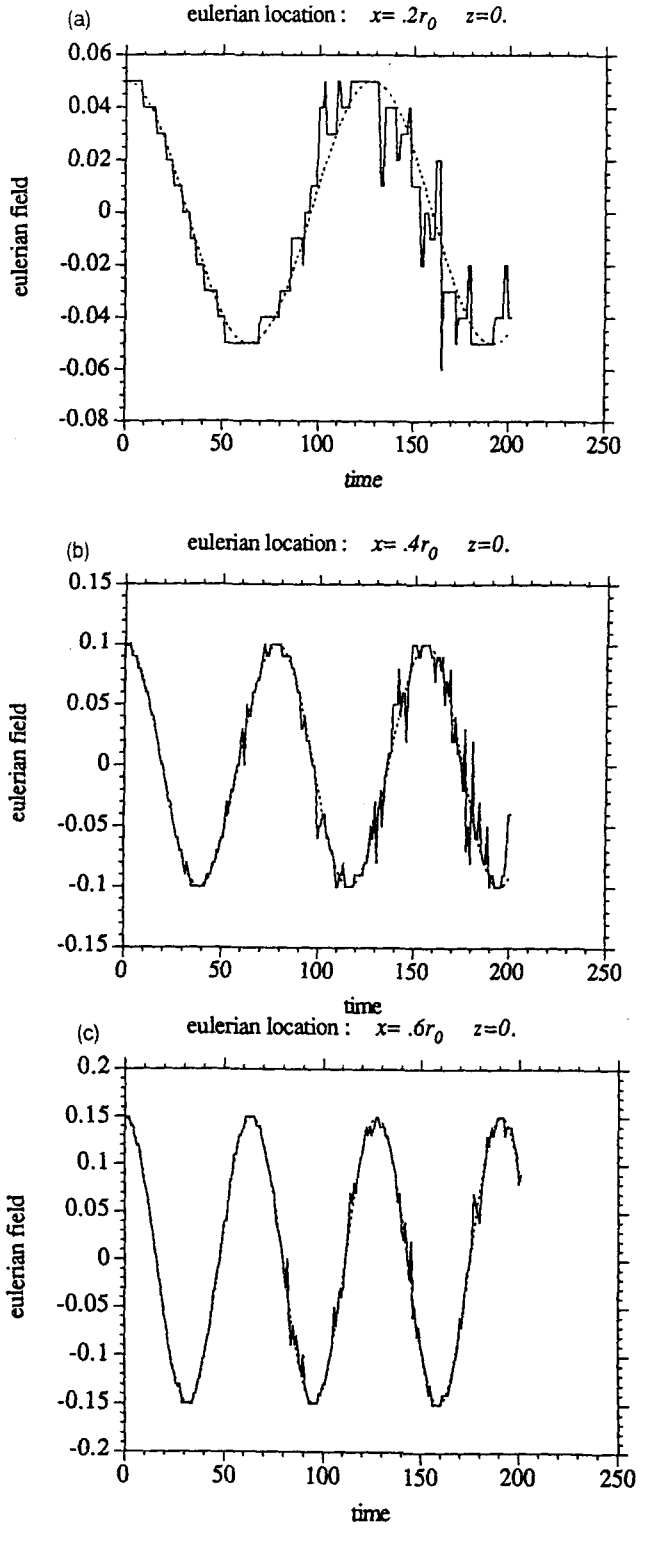

Figure 7. Whirl flow. Advection by the whirl flow of the initial field $\phi = x$. Flow parameters and geometry are defined in the text. The diagrams compare the evolution of analytical values (dashed line) and the numerical values (solid line) of the corresponding Eulerian field at the Eulerian locations indicated in the figure. The value of r_0 is 0.25. The numerical values of the Eulerian field are computed with CP^L regridding (see Section 4.3). The differences between (1) the analytical and numerical Eulerian fields, and (2) the Eulerian fields at the locations (a), (b) and (c), are explained in the text.

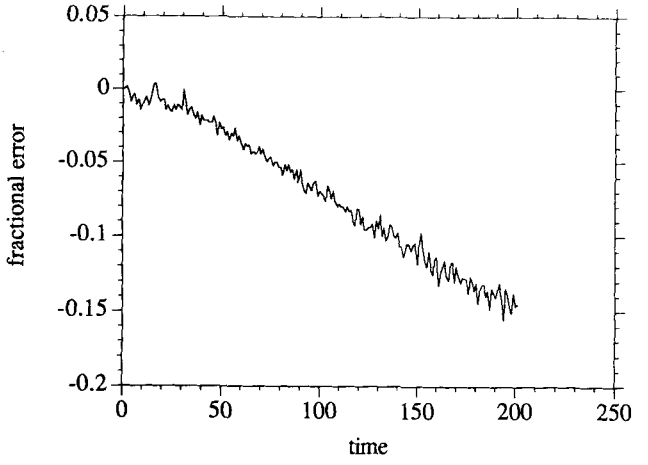

Figure 8. Whirl flow. Evolution through time of the fractional error ε defined in the text. This error is a measure of the non-conservation of the Eulerian field. It is due to the low-pass filter effect of the Eulerian grid on a Lagrangian field which develops structures at progressively smaller scales. The linear variation observed is explained in the text.

approached. The error therefore varies from a larger amplitude–smaller frequency in Fig. 7(a) to a smaller amplitude–higher frequency in Fig. 7(c).

We show in Fig. 8 the variation in time of the 0th order moment of the field, which should be zero for the incompressible whirl flow. We define the fractional error:

$$\varepsilon = \frac{M^0(t) - M^0(0)}{M^0(0)},$$

where $M^0(t)(M^0(0))$ is the integral of the Eulerian field $\hat{\phi}^E$ at time t (at time $t = 0$). The fractional error increases linearly with time (Fig. 8) and this confirms our previous analysis of the regridding error. The short-frequency component corresponds to the selection of adjacent closest neighbours in the interpolation of the field to the Eulerian node. The particular field chosen has a zero curl symmetry, which explains why the periodicity of the flow does not show in the time evolution of the field integral and fractional error. For initial fields having other symmetries, like the field $|x|$, a periodic component would be superposed on the linear trend in time.

We speculate that the increase of the regridding error is polynomial (exponential) in time for systems with zero (positive) Lyapounov exponents. In the case of the general unsteady subduction model, the rheological and boundary conditions under which the flow has a positive Lyapounov exponent are not known. In all the subduction models refered to in this paper, the flow has only weak mixing properties (Ottino 1989).

An M flow example: quasi-convection flow

In this example the regridding not only performs field advection but also has a feedback effect on the dynamics. More precisely, this example uses thermomechanical coupling, in the Boussinesq approximation, between a linear viscous Stokes (and not Navier–Stokes) flow and a temperature field that evolves by conduction and advection, which explains our terminology 'quasi-convection'. This example is given because it is a better illustration and test of regridding than the subduction model for several reasons.

(1) All experiments with the subduction model have so far assumed an infinite Peclet number. The quasi-convection problem provides a test of the thermomechanical coupling which will be used in the next versions of the subduction models. This will, in particular, enable the computation of P–T–t (pressure-temperature-time) paths with material advection and thermal conduction fully included.

(2) No reference solution exists for a subduction model using regridding which couples temperature or strain to the rheology. By contrast, a large number of numerical experiments exist for convection flows and the results shown here could be compared to results obtained from other methods.

(3) In the quasi-convection model the velocity field is very sensitive to the regridding, especially for Peclet numbers of order 1 or less. Indeed, velocities are driven by density gradients created by the combination of temperature advection and diffusion. No scale is given to the velocity field by a kinematical boundary condition and the regridding error rapidly affects the dynamics.

(4) The quasi-convection model achieves stationary velocity and temperature fields after an initial 'spin-up' phase. From then on variation in time is eliminated as a source of error in the advection of Lagrangian nodes and errors in the regridding can therefore be attributed to spatial interpolation. Errors due to the Eulerian motion are also eliminated because the Eulerian grid is fixed in the present model.

Dimensionless parameters are used in this model. A symmetric heat flux varying from 1.08×10^{-3} to a peak value of 3.25×10^{-3} is applied to the base of a rectangular box of dimensions $L = 1$ and $H = 0.4$. The thermal conductivity, specific heat, acceleration due to gravity, initial density and uniform viscosity are respectively:

$k = 5 \times 10^{-4}$

$c = 1.0$

$g = 10.$

$\rho_0 = 1.0$

$\mu = 0.2.$

The temperature, θ, is assumed to control density by a linear relation,

$\rho = \rho_0(1 - \alpha\theta),$

with $\alpha = 0.1$. These parameters were chosen to allow the onset of convection and correspond on a stability diagram (Turcotte & Schubert 1982) to a Rayleigh number $\mathrm{Ra} \sim 1200$ and a dimensionless wavenumber 2.5. The mechanical boundary conditions are free slip on all sides and the thermal boundary conditions, other than the basal flux, are zero temperature on the top surface and lateral insulation. No exact analytical solution exists for this problem, but an order of magnitude solution is provided by the boundary-layer theory of convection that predicts a maximum velocity:

$$\mathbf{v}_0 \sim 2.71 \frac{k}{\rho_0 c H} R_a^{2/3} \sim 3 \times 10^{-2}$$

in the optimum case $L = 2H$. The corresponding value of the maximum stationary velocity in the numerical solution is 1.4×10^{-2}. The agreement is reasonable, given the approximative character of the boundary-layer theory, the non-optimum wavenumber used and the use of Stokes rather than Navier–Stokes equilibrium equations. The Peclet number $k/\mathbf{v}H$ varies from approximately 0.1 to 1, in the convective cores, and the solution is therefore not dominated by conduction. The asymptotic stationary fields (temperatures and velocities) correspond to an equilibrium between advection and diffusion.

The thermal diffusion of temperatures is solved on a Eulerian grid of low resolution (50×20) and closest-point interpolation and injection are used to solve the temperature-advection problem with an initial grid of 200×20 Lagrangian particles and a resolution $\delta_x = \delta_z$ for the injection, equal to a quarter of the Eulerian resolution. The flow is followed in time for 1000 steps ($\Delta t = 1.$), or approximately nine full rotations of the material layers peripheral to the convective cores.

We compute and show (Figs 9 to 11) several estimates of the regridding error by inspecting the temporal and spatial elements of symmetry of the solution. The exact Eulerian (Lagrangian) temperature-velocity solution is stationary (periodic in time), therefore, the temporal variation of the numerical solution and its aperiodicity provide a measure of the noise introduced by the regridding.

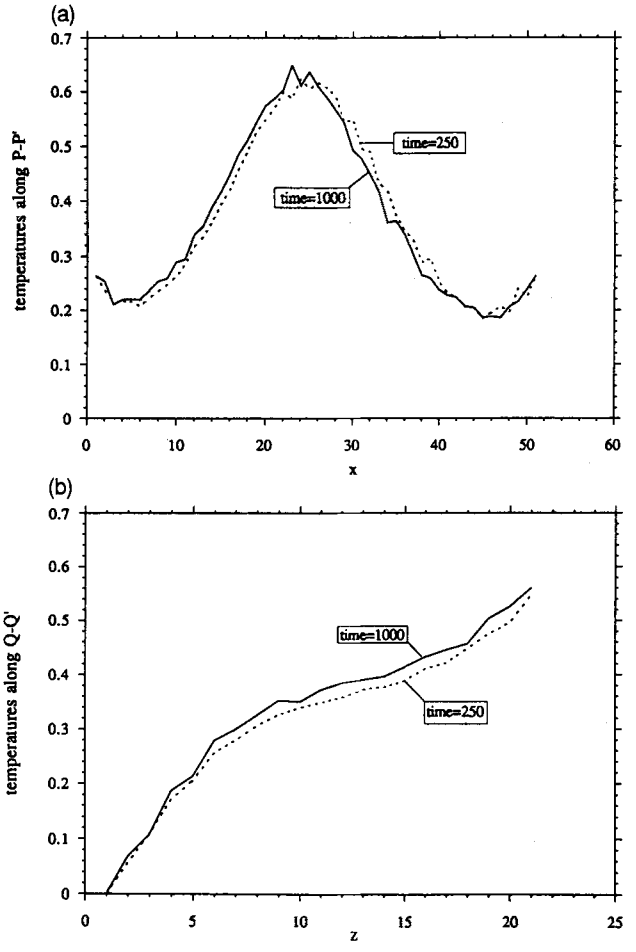

Figure 9. Quasi-convection flow. Temperature profiles at time $t = 250$ (dashed lines) and $t = 1000$ (solid lines) along the lines (a) P–P', and (b) Q–Q' shown in Fig. 10(b). Temperature values are normalized by the maximum temperature $T_{\max} = 1.9$, as in Figs 10(b) and 11.

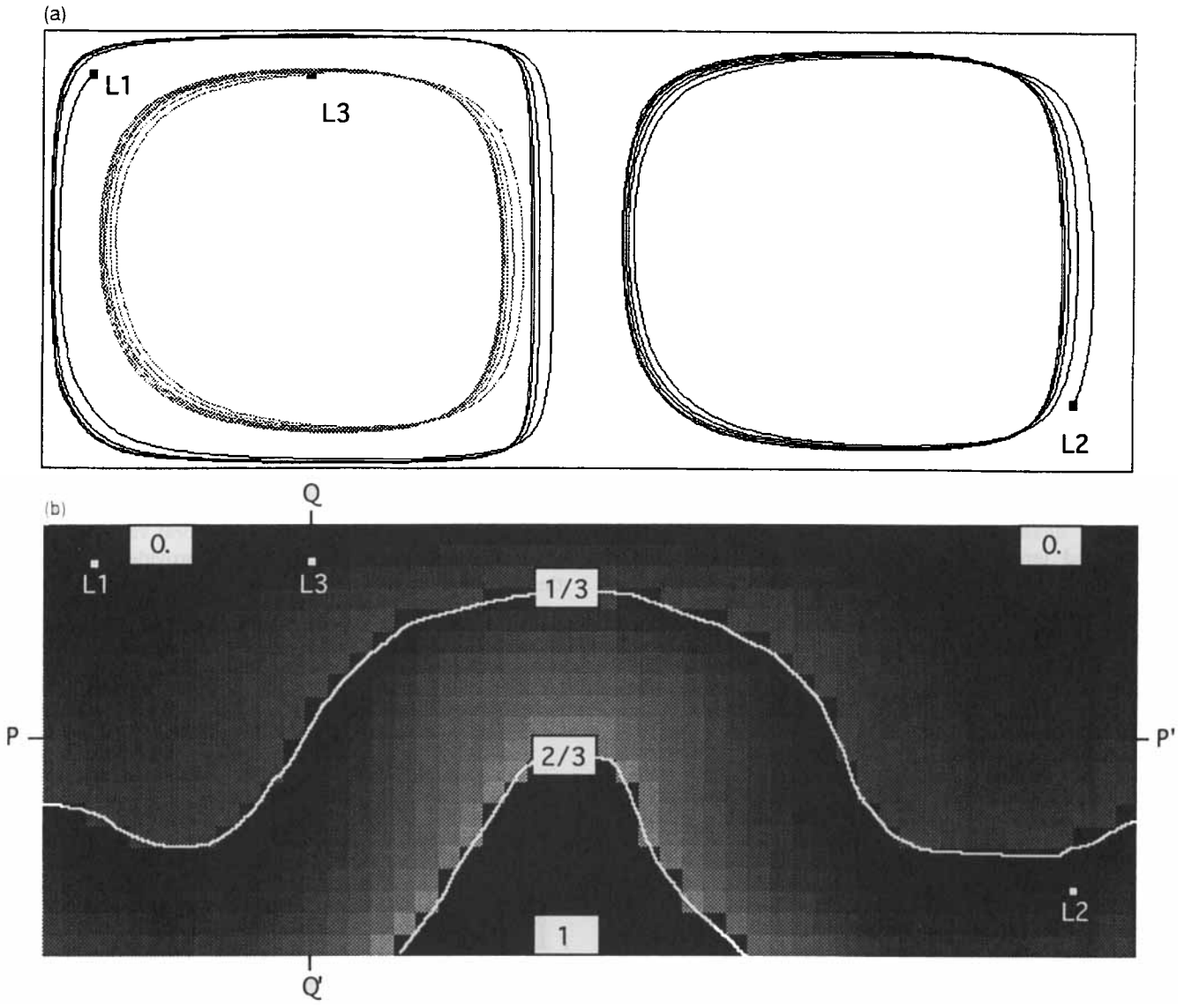

Figure 10. Quasi-convection flow. (a) Shows the Eulerian domain of the flow (box) and the trajectories followed by three selected Lagrangian particles L1, L2, L3 during the time interval [0, 1000]. The initial positions of L1, L2, L3 are indicated by small black boxes. The final positions at time $t = 1000$ are not shown. (b) Schematic representation of the Eulerian temperature spatial distribution at time $t = 1000$. Normalized temperatures values are shown in the white boxes: 0. is the surface temperature, the temperature is maximum (1.) at the location shown, and approximate isotemperature contours for $T = 1/3$ and $T = 2/3$ are shown. The grey tone values are not proportional to the temperatures.

(1) The 0th moment (as defined in the previous section) of temperature is varying in the stationary phase (after 100 steps) between 0.26737 and 0.2615 with a very small average temporal trend (the regression line is $\theta = .26737 - 3.09 \times 10^{-7} t$). This result confirms that the temperature field is conserved.

(2) Figure 9 shows the temperature profiles on the vertical line $x = 0.25$ across the left convective core (Fig. 9a) and on the horizontal line $z = 0.2$ passing through the two cores (Fig. 9b). In each case, only small wavelength oscillations of the order of the Eulerian resolution have been superimposed on the solution by the regridding. The difference between the profiles at time $t = 250$ and $t = 1000$ is of the order of the temperature difference across one Eulerian element.

(3) The short-wavelength oscillations and numerical non-stationarity of the temperature have a feedback effect on the velocity field and, therefore, on the trajectories of Lagrangian particles. Fig. 10(a) shows these trajectories of three selected Lagrangian particles. The trajectories are only quasi-periodic and slightly diffuse in space on a distance of the order of the Eulerian resolution. This numerical diffusion increases with curvature. We observe, without explanation, that this diffusion is more pronounced along the parts of the trajectories corresponding to predominantly vertical motion. Fig. 10(b) shows for reference the x–z distribution of the quasi-stationary temperature field in equilibrium with convection and diffusion.

(4) Fig. 11 shows the time series corresponding to the evolution of the temperature for the same selected

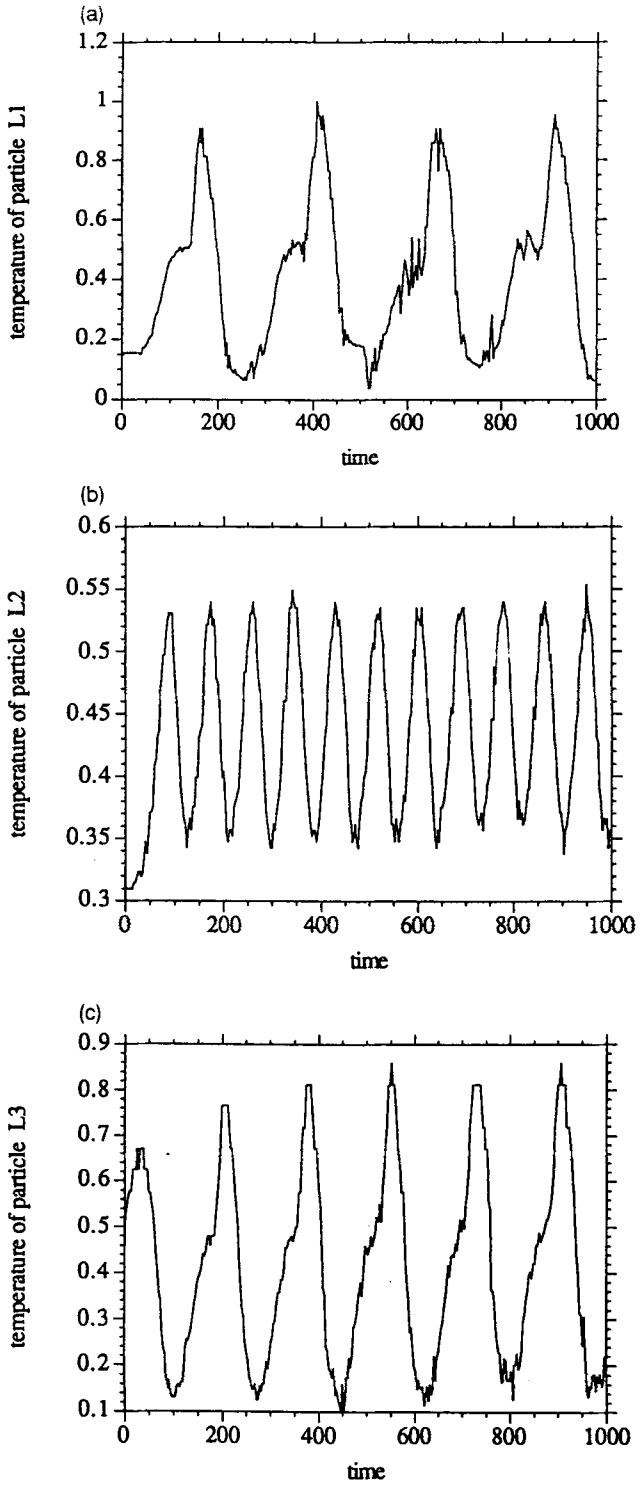

Figure 11. Quasi-convection flow. Variation through time of the normalized temperature for the three Lagrangian particles (a) L1, (b) L2, (c) L3 shown in Fig. 10. The noise levels and quasi-periodicity in these time series is explained in the text.

Lagrangian particles. These particles are quasi-periodically advected through the quasi-stationary temperature field. These time series would be smooth and perfectly periodic for an exact solution. The numerical solutions shown here incorporate errors due to the slight unstationarity of the Eulerian velocity field along the Lagrangian trajectories. They also include the error due to the slight unstationarity of the Eulerian temperature field along the Lagrangian trajectories. For these reasons, they are not strictly periodic and a fluctuation of approximately 5 per cent (which is the Eulerian resolution in temperatures as observed above) is observed on the amplitudes of each series. The maximum noise level in these series correspond to the passage of the Lagrangian particles in the zones of high temperature gradients, where the regridding error has a maximum amplitude.

These qualitative tests show that the quasi-convection calculations exhibit only high-frequency/short-wavelength errors and give overall acceptable results.

In this section the ALE-R method was used to solve an infinite Prandtl number thermal-convection problem. Similar methods have been used for the solution of incompressible (Christiansen 1973) or compressible Navier–Stokes equations. In these cases, however, special techniques have to be introduced to prevent excessive diffusion of momentum (Brackbill & Ruppel 1986).

6 DISCUSSION AND CONCLUSION

This paper has presented the basic framework for the subduction model (SM) of compressional orogens and has described the numerical methods used in SM and other applications of the model to geodynamical problems. Here we review the applicability of this type of computation to SM and propose more general problems, relevant to geodynamics, for which the ALE-R techniques might be used. We conclude with an assessment of the numerical methods and review some future developments of this work.

6.1 ALE-R computations related to geodynamics

ALE-R computations and the subduction model

SM is characterized by a particular set of boundary conditions while other model attributes, like the viscoplastic rheology, the coupling with surface processes and/or isostasy, are less specific to SM. The ALE-R technique is well adapted to these boundary conditions, which contribute to the presence of localized zones of high deformation in the domain of the flow. The usefulness of the numerical ALE-R simulations to SM is illustrated by the following points.

(1) SM can be used to understand aspects of the dynamics of accretionary wedges. There is a good agreement between the geometrical predictions of the model computed by ALE-R simulation and the exact critical wedge theory (Dahlen 1984) when a cohesionless frictional (Coulomb) rheology is used. In particular, the computed pro-wedge develops into a critical wedge of constant slope and the value of this slope is close to that of the analytical solution. ALE-R simulations also indicate that the computed retro-wedge may develop with the maximum critical taper angle (S. Willett, personal communication).

(2) SM possibly represents a unified mechanical model for natural compressional orogens in which style variations reflect crustal response. The range of ALE-R simulations encompasses this broad variety of problems, and more. Correspondingly, the complexity of the rheology and

boundary conditions makes it difficult to design tests for the numerical accuracy of general SM models. We therefore cannot draw conclusions on the quality of the numerical results in these cases and related analogue models offer the best prospect for tests. The numerical tests that have been presented above (Section 5) do, however, give some degree of confidence in each element of the ALE-R method.

(3) ALE-R simulations of complex SM may nevertheless be useful because they allow the determination of quantities that would be more difficult (if not impossible) to obtain by analytical, physical analogue, or other less-adapted numerical methods. Examples of such quantities are the spatial stress distribution, the topography, and Lagrangian time series: that is, the evolution in time of physical quantities for a Lagrangian particle as it is advected by the flow.

P-T-t paths are Lagrangian time series that can be related to the metamorphic processes that transform rocks when they travel through an orogen (Jamieson & Beaumont 1988; Barr & Dahlen 1989). When erosion rates are significant by comparison with tectonic uplift rates, exhumation of the rocks produces high thermal gradients. These can only be resolved in the computed Lagrangian time series if the computation includes temperature calculations in the finite Peclet number range. The principle of this computation using the ALE-R formulation has been outlined in the discussion of the quasi-convection flow (Section 5.3) and will be used in future SM models to calculate P-T-t paths.

The evolution of strain, or strain path, represent another class of Lagrangian time series which can be computed by ALE-R simulations. Strain paths are used in structural geology to understand the shearing processes operating in a deforming zone (Passchier 1988, for example). The observation of rocks at small scale (10 m to the scale of the polycrystalline aggregates) is used to reconstruct the strain path followed by rocks. We intend to use ALE-R simulations of SM to decide whether the computed strain Lagrangian time series are consistent with averages (at scales of the order of the Eulerian resolution) of these smaller-scale observations. It is doubtful, however, that the simplified rheologies currently used in the SM models will reproduce these average strains. Deformation complexity exists at all scales and this behaviour, as opposed to scalar quantities like those associated with PTt, is not resolved by our current models.

ALE-R computations and analogue models

Various materials varying from plaster (since Cadell 1889) to sand (Davis *et al.* 1983; Malavieille 1984) and layered composites (Lie *et al.* 1992) have been used in analogue 'sandbox' experiments that are related to SM (Malavieille 1984) and backstop models (Davis *et al.* 1983; Liu *et al.* 1992; Wang & Davis 1992; Byrne, Wang & Davis 1993). These experiments confirm and validate some of the results obtained with the present model, for example the prediction of the slope of compressive sand wedges. The complex rheology of sand makes it difficult for detailed comparisons to be made between our current incompressible Coulomb models and the sand experiments. It remains to be determined whether ALE-R numerical simulations with Granta–Gravel or Cam–Clay rheologies (Section 3.2) which approximate the mechanical properties of sand will yield finer-scale features seen in the sandbox experiments. Analogue experiments are important for the testing and development of the numerical methods and this is particularly true when the rheological properties of the materials are fully characterized and are not too complex. The analogue models are valuable regardless of the applicability of sand or other rheologies to the earth.

ALE-R computations for more general models

ALE-R computations can be extended to apply to more general models.

(1) They could, for example, be used in models at a lithospheric as opposed to crustal scale. Flow models have been used with non-linear viscous rheologies in extensional numerical experiments at the lithospheric scale (Christensen 1992). Such models assume no kinematical boundary conditions at the base of the lithosphere and similar models with stress boundary conditions could be designed in compression.

(2) They could be used in 3-D models, for example in the simulation of orogens created by transpression between plates (Braun, personal communication). This would usefully complement and complete the vertical plane strain and horizontal thin sheet models, which have a restricted range of validity.

(3) It may also be possible to incorporate rheologies that have an elastic component. It is, however, premature at this stage to comment on the efficiency of ALE-R techniques in this category of problems, where regridding stresses is necessary.

6.2 ALE-R computations; conclusions

Our first motivation for the development of ALE-R methods resulted from difficulties encountered with earlier numerical simulations of compressional orogens. These simulations used a UL formulation and elasto-viscoplastic rheologies. The pseudo-viscous flow approach in an ALE formulation (Zienkiewicz 1977) was tested as an alternative and proved to be satisfactory for WM flows like incompressible Coulomb plastic flows (Willett 1992). The need to compute the material deformation suggested the need to initialize and track a Lagrangian grid. Finally, the extension to M flows was made possible by the addition of the regridding. The result is the ALE-R method, which may be applied to a variety of flow simulations.

Modularity of the method

ALE-R computations use a series of modules some of which are listed below.

- Finite-element modules (1-D flexure code, 2-D velocity-pressure incompressible Stokes 2-D diffusion code).
- Surface-tracking module (1-D cubic-spline interpolation).
- Eulerian remeshing module (vertical linear interpolation).

- Linear solver module (Linpack symmetric positive-definite system solver).
- Non-linear solver module (direct iteration on effective viscosities).
- Lagrangian grid to Eulerian grid regridding module (consistent Lagrangian advection, closest point interpolation, Lagrangian nodes injection.

Each of these modules has been used for some time in fluid-flow computations and we have referred in Section 2 to a few of the relevant works. The computations in Christensen (1992) have many aspects in common with the ALE-R as described above but differ in the module characteristics. Poliakov & Podladchikov (1992) have developed numerical techniques that are even more similar in their organization and characteristics to ALE-R.

Although the modules are not necessarily optimum, they are simple and reasonably efficient for models which do not require highly accurate solutions. Their relative independence also provides flexibility. For example:

- adaptive-node movement techniques (Hawken *et al.* 1991) could be used in the Eulerian remesher provided the Eulerian motion is continuous, and this would not affect the ALE-R structure;
- the velocity-pressure FE module may be replaced by a FE module using displacements;
- all modules may be restructured in higher dimensions and be vectorized.

Developments of the method

We wish to continue to develop the ALE-R method in essentially two directions.

(1) The method should include a broader range of boundary conditions and rheologies. Boundary conditions should be designed to give a better model of the physics of lithospheric subduction or allow larger-scale computations including the mantle. Extension or cycles of extension/compression should be tested. In 3-D, compressive-to-transpressive experiments will be performed.

Regarding rheologies, we wish to compare results from plane-strain computations of SM using elasto-viscoplasticity with corresponding results using pseudo-viscous flows. We will also test non-linear solver modules based on the constant strain-rate algorithm (Woodward 1980) in combination with plastic predictors, by contrast with the elastic predictor approach usually employed. Tests already performed with elastic predictors in a hyperelastic formulation of Cam–Clay have shown convergence problems for SM models. This motivates a search for new algorithms. The covergence of the direct iteration module will also be studies for plastic rheologies that include softening and hardening.

(2) The method should be optimized for higher resolution computations. A vectorized implementation of the ALE-R structure is necessary for high resolution and 3-D computations using vector or parallel processors. All the elements of the methods presented here can be restructured in 3-D and this has been confirmed by a few preliminary tests. Efficient 3-D computations need, however, a significant optimization of each module, and this has not been addressed in this work. The promising numerical techniques developed by Braun (1993, 1994) are a very significant step in this direction.

ACKNOWLEDGMENTS

This work was funded by N.S.E.R.C. Operating and Lithoprobe Supporting Geoscience grants to Christopher Beaumont. Lithoprobe contribution No. 621. This work is the result of a collective effort by the Geodynamics group at Dalhousie University to improve modelling tools. Many thanks to C. Beaumont and S. Willett who have contributed as much as the author to all the essential aspects of the methods. Thanks to J. Hamilton for her patience and constructive help. We acknowledge J. Braun for many fruitful and clever discussions.

REFERENCES

Babuska, I., 1973. The finite element method with Lagrange multipliers, *Numer. Math.*, **20,** 179–197.

Barr, T.D. & Dahlen, F.A., 1989. Brittle frictional mountain buliding 2, thermal structure and heat budget, *J. geophys. Res.*, **94,** 3923–3948.

Beaumont, C. & Quinlan, G., 1994. A geodynamic framework for interpreting crustal-scale seismic-reflectivity patterns in compressional orogens, *Geophys. J. Int.*, **116,** 754–783.

Beaumont, C., Fullsack, P. & Hamilton, J., 1992. Erosional control of active compressional orogens, in *Thrust Tectonics,* pp. 19–31, ed. McClay, K.R., Chapman and Hall, London.

Beaumont, C., Fullsack, P. & Hamilton, J., 1994. Styles of crustal deformation in compressional orogens caused by subduction of the underlying lithosphere, in *Proc. 5th Int. Symp. Seism. Reflect. Prob. Contin. Marg.*, eds Clowes, R. & Green, A., *Tectonophysics,* **232,** 119–132.

Bird, P., 1989. New finite element techniques for modeling deformation histories of continents with stratified temperature dependent rheology, *J. geophys. Res.*, **94,** 3967–3990.

Brackbill, J.V. & Ruppel, H.M., 1986. FLIP. A method for adaptively zones, particle-in-cell calculations of fluid flows in two dimensions, *J. Comput. Phys.*, **65,** 314–343.

Braun, J., 1993. Three dimensional numerical modeling of compressional orogens: thrust geometry and oblique convergence, *Geology,* **21,** 153–156.

Braun, J., 1993. Three dimensional numerical simulations of crustal-scale wrenching using a non-linear failure criterion, *J. Struct. Geol.*, **16,** 1173–1186.

Braun, J. & Beaumont, C., 1987. Styles of continental rifting: results from dynamic models of lithospheric extension, in *Sedimentary Basins and Basin-Forming Mechanisms,* **12,** pp. 241–258, eds Beaumont, C. & Tankard, A. J., Can. Soc. of Petrol. Geol.

Brezzi, F., 1974. On the existence, uniqueness and approximation of saddle-point problems arising from Lagrange multipliers, *Rairo,* **8,** 129–151.

Byrne, D.E., Wang, W. & Davis, D.M., 1993. Mechanical role of backstops in the growth of fore arcs, *Tectonics,* in press.

Cadell, H.M., 1889. Experimental Researches in Mountain Building, *Trans. R. Soc. Edinb.*, **1,** 337–357.

Chabard, J.P., Daubert, O., Gregoire, J.P. & Hemmerich, P., 1987. A finite element code for the efficient computation of turbulent industrial flows, *Numer. Method Laminar Turbulent Flow,* **5,** 672–683.

Christiansen, J.P., 1973. Numerical simulation of hydrodynamics by the method of point vortices, *J. Comput. Phys.*, **13,** 363–379.

Christensen, U., 1984. Convection with pressure- and temperature-

dependent non-Newtonian rheology, *Geophys. J. R. ast. Soc.*, **77,** 343–384.

Christensen, U.R., 1992. An Eulerian technique of thermomechanical modeling of lithospheric extension, *J. geophys. Res.*, **97,** 2015–2036.

Collins, I.F., 1990. Plane strain characteristic theory for soils and granular materials with density dependent yield criteria, *J. Mech. Phys. Solids,* **38,** 1–25.

Coulomb, C.A., 1773. Sur une application des règles de maximis et minimis a quelques problèmes de statique relatifs à l'architecture, *Acad. R. Sci. Mem. Math. Phys. Par Divers Savans,* **7,** 343–382.

Dahlen, F.A., 1984. Noncohesive critical Coulomb wedges: an exact solution, *J. geophys. Res.*, **89,** 10125–10133.

Dahlen, F.A. & Barr, T.D., 1989. Brittle frictional mountain building 1, deformation and mechanical energy budget. *J. geophys. Res.*, **94,** 3906–3922.

Davis, D., Suppe, J. & Dahlen, F.A., 1983. Mechanics of fold and thrust belts and accretionary wedges, *J. geophys. Res.*, **88,** 1153–1172.

Dunbar, J.A. & Sawyer, D.S., 1988. Continental rifting at pre-existing lithospheric weaknesses, *Nature,* **333,** 450–452.

Dunbar, J.A. & Sawyer, D.S., 1989. How pre-existing weaknesses control the style of continental breading, *J. Geophys. Res.*, **94,** 7278–7292.

Emerman, S.H. & Turcotte, D.L., 1983. A fluid model for the shape of accretionary wedges, *Earth planet. Sci. Lett.*, **63,** 379–384.

England, P. & McKenzie, D., 1982. A thin viscous sheet model for continental deformation, *Geophys. J. R. astr. Soc.*, **70,** 295–321.

Fung, O.C., 1977. *The Finite Element Method,* McGraw-Hill, New York.

Harlow, F.H. & Welch, J.E., 1965. Numerical calculation of time-dependent viscous incompressible flow of fluid with free surface, *Phys. Fluids,* **8,** 2182–2189.

Hawken, D.F., Gottlieb, J.J. & Hansen, J.S., 1991. Review of some adaptive node-movement techniques in finite-element and finite-difference solutions of partial differential equations, *J. Comput. Phys.*, **95,** 254–302.

Hirt, C.W., Amsden, A.A. & Cook, J.L., 1974. An arbitrary lagrangian-eulerian computing method for all flow speeds, *J. Comput. Phys.*, **14,** 227–253.

Hobbs, B.E., Mülhaus, H.B. & Ord, A., 1990. Instability, softening and localization of deformation, in *Deformation Mechanisms, Rheology and Tectonics,* **54,** pp. 143–165, eds Knips, R.J. & Rutter, E.H., Geol. Soc. Spec. Publ., London.

Houseman, G. & England, P., 1986. Finite strain calculations of continental deformation 1. Method and general results for convergent zones, *J. geophys. Res.*, **91,** 3651–3663.

Jaeger, J.C. & Cook, N.G.W., 1976. *Fundamentals of Rock Mechanics,* Chapman and Hall, London.

Jamieson, R.A. & Beaumont, C., 1988. Orogeny and metamorphism: a model for deformation and pressure-temperature-time paths with application to the central and southern Appalachians, *Tectonics,* **7,** 417–445.

Johnson, D. & Beaumont, C., 1994. Preliminary results from a planform kinematic model of orogen evolution, surface processes and the development of clastic foreland basin stratigraphy, in *Stratigraphic Evolution of Foreland Basins,* eds Dorobek, S. & Ross, G.M., Soc. Econ. Paleo. Mineral. Spec. Publ., no. 52, in press.

Ladyzhenskaya, O.A., 1969. *The Mathematical Theory of Viscous Incompressible Flows,* Gordon & Breach, New York.

Lenardic, A. & Kaula, W.M., 1993. A numerical treatment of geodynamic viscous flow problems involving the advection of material interfaces, *J. geophys. Res.*, **98,** 8243–8260.

Liu, Huiqi, McClay, K.R. & Powell, D., 1992. Physical models of thrust wedges, *Thrust Tectonics,* pp. 71–81, ed. McClay, K.R., Chapman and Hall, London.

Malavieille J., 1984. Modélisations expérimentale des chevauchements imbriqués: application aux chaînes de montagnes, *Bull. Soc. Geol. France,* (7), **XXVI,** 129–138.

Malkus, D.S. & Hughes, T.J.R., 1978. Mixed finite element methods—one point and selective integration techniques: a unification of concepts. *Comput. Meths. appl. Mech. Eng.*, **15,** 63–81.

Mandl, G., 1988. *Mechanics of Tectonic Faulting: Models and Basic Concepts,* Elsevier, Amsterdam.

McMeeking, R.M. & Rice, J.R., 1975. Finite element formulations for problems of large elastic-plastic deformation, *Int. J. Solids Struct.*, **11,** 601–616.

Ottino, J. M., 1989. *The Kinematics of Mixing: Stretching Chaos and Transport,* Cambridge University Press, Cambridge.

Park, K.C., 1984. Locking, spurious mechanisms, and pressure divergence in penalty finite element methods for Stokes flow problems, *Comput. Meths. appl. Mech. Eng.*, **47,** 315–330.

Passchier, C.W., 1988. Analysis of deformation paths in shear zones, *Geol. Runds.*, **77,** 309–318.

Perzyna, P., 1988. Temperature and rate dependent theory of plasticity of crystalline solids, *Rev. Phys. Appl.*, **23,** 445–459.

Poliakov, A. & Podladchikov, Y., 1992. Diapirism and topography, *Geophys. J. Int.*, **109,** 533–564.

Prager, W., 1956. Finite Plastic Deformation, in *Rheology, Theory and Applications,* **1,** pp. 63–96, ed. Eirich F.R., Academic Press, New York.

Press, W.H., Flannery, B.P., Teukolsky, S.A. & Vetterling, W.T., 1986. *Numerical Recipes: The Art of Scientific Computing,* Cambridge University Press, Cambridge.

Ranalli, G., 1987. *Rheology of the Earth: Deformation and Flow Processes in Geophysics and Geodynamics,* Allen and Unwin, Boston.

Schofield, A.N. & Wroth, C.P., 1968. *Critical State Soil Mechanics,* McGraw-Hill, London.

Sedov, L., 1975. *Mécanique des Milieux Continus,* Editions Mir, Moscow.

Shreve, R.L. & Cloos, M., 1986. Dynamics of sediment subduction, melange formation, and prism accretion, *J. geophys. Res.*, **91,** 10229–10245.

Spencer, A.J.M., 1964. A theory of the kinematics of ideal soils under plane strain conditions, *J. Mech. Phys. Solids,* **12,** 337–351.

Stockmal, G.S., 1983. Modeling of large-scale accretionary wedge deformation, *J. geophys. Res.*, **88,** 8271–8287.

Tapponier, P. P. & Molnar, P., 1976. Slip line field theory and large scale continental tectonics, *Nature,* **264,** 319–324.

Turcotte, D.L. & Schubert, G., 1982. *Geodynamics: Applications of Continuum Physics to Geological Problems,* John Wiley and Sons, New York.

Vilotte, J.P., Madariaga, R., Daignières, M. & Zienkiewicz, O.C., 1986. Numerical study of continental collision: influence of buoyancy forces and an initial stiff inclusion, *Geophys. J. R. astr. Soc.*, **84,** 279–310.

Wang, W.H. & Davis, D.M., 1992. Sandbox model simulation of fore-arc evolution *EOS, Trans. Am. geophys. Un.*, **73,** 293.

Willett, S., 1992. Dynamic and kinematic growth and change of a Coulomb wedge, in *Thrust Tectonics,* pp. 19–31, ed. McClay, K.R., Chapman and Hall, London.

Willett, S., Beaumont, C. & Fullsack, P., 1993. A mechanical model for the tectonics of doubly-vergent compressional orogens, *Geology,* **21,** 371–374.

Woodward, D.J., 1980. Visco-elastic finite element analysis in tectonic systems, *Geophys. J. R. astr. Soc.* **63,** 285–288.

Zienkiewicz, O.C., 1977. *The Finite Element Method,* McGraw-Hill, New York.

Zienkiewicz, O.C. & Godbole, P.N., 1975. Penalty function approach to problems of plastic flows of metals with large surface deformations, *J. Strain Anal.*, **10,** 180–183.

APPENDIX: ADVECTION AND REGRIDDING

The velocity of a Lagrangian particle (represented by a square at location X^L), is determined (Fig. A1, left) by mapping the Eulerian element I (containing the particle) onto a reference element (Fig. A1a, right). The reference coordinates of the Lagrangian particle are used to interpolate its velocity from the velocity at the Eulerian nodes (circles at locations X_1^E, X_2^E, X_3^E, X_4^E) defining the element I.

Fig. A1b shows the process of simultaneous advection over a time step of the Lagrangian particle (square) and of the Eulerian nodes (circles). Arrows represent here the incremental displacements between the old (white) and updated (black) locations. Eulerian nodes are moving with Eulerian velocities, here vertical, which allow the grid to conform to the deformed domain (Fig. A1b, right) at the end of the time step; the corresponding Eulerian displacements are u_1^E, E_2^E, u_3^E, u_4^E. The Lagrangian particle moves with the velocity determined in (a) and is advected by a displacement $u^L = v^L \Delta t$. Because the Eulerian motion is not material, the Eulerian cell containing the Lagrangian particle may be different before and after advection. The Eulerian cell I containing the particle is therefore updated through a local search process. At the same time, the number of the Lagrangian particle closest to each Eulerian node of the element is updated, if needed.

When these steps have been completed for all Lagrangian particles (Fig. A1c), each Eulerian node E (black circle) is associated to its closest Lagrangian particle CP(E) (black square) and all fields carried by the particle CP(E) are transferred to the Eulerian value of the field at E. The reverse operation, from Eulerian nodes to Lagrangian nodes, is given by consistent interpolation.

Last, when the Lagrangian cloud is too sparse, e.g. when the distance d(E, CP(E)) between a Eulerian node E and its closest Lagrangian node CP(E) exceeds some limit R, a new Lagrangian particle, NEW, is introduced ('injected') by bisecting the positions and the field values at E and CP(E).

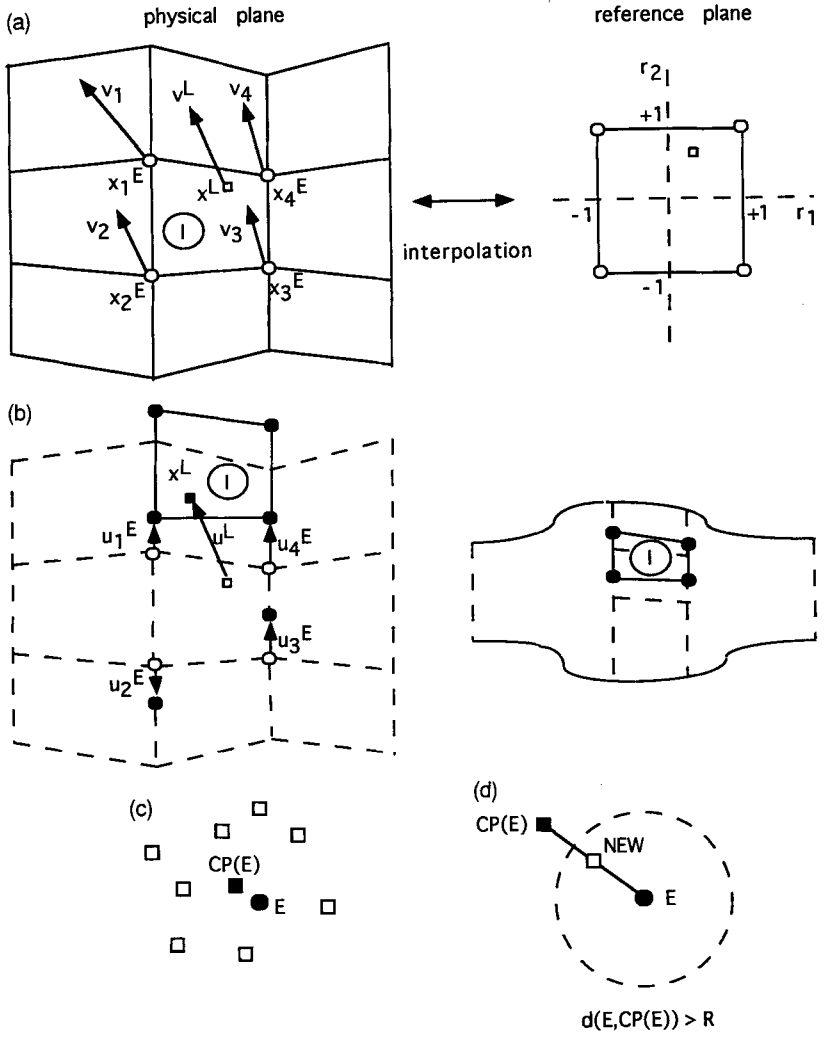

Figure A1. Advection and regridding method. (a) Computation of the Lagrangian velocities. (b) Eulerian and Lagrangian advection. (c) Closest point regridding. (d) Injection of new Lagrangian particles. Explanations and details are given in Appendix and in Sections 4.2 and 4.3, respectively.